Superfluid turbulence and stability of BEC: using the Gross-Pitaevskii equation

Marc Brachet [a]

[a] *Laboratoire de Physique Statistique, CNRS UMR 8550, École Normale Supérieure, 24 rue Lhomond, 75231 Paris Cedex 05, France*

Abstract

The Gross-Pitaevskii equation, also called the nonlinear Schrödinger equation (NLSE), describes the dynamics low-temperature superflows and Bose-Einstein Condensates (BEC). We review some recent NLSE-based numerical studies of superfluid turbulence and BEC stability. The relations with experiments are discussed.

Key words:

Contents

1 Introduction

The present paper is a review of results, obtained in the last 10 years or so, by numerically studying the nonlinear Schrödinger equation (NLSE). Direct numerical simulations (DSN) and branch-following methods were extensively used to investigate the dynamics and stability of NLSE solutions in 2 and 3 space dimensions.

Much work has been devoted to the determination of the critical velocity at which superfluidity breaks into a turbulent regime [1]. A mathematical model of superfluid ^{4}He, valid at temperatures low enough for the normal fluid to be negligible, is the nonlinear Schrödinger equation (NLSE), also called the Gross-Pitaevskii equation [2–4]. In a related context, dilute Bose-Einstein condensates (BEC) have been recently produced experimentally [5–7]. The dynamics of these compressible nonlinear quantum fluids is accurately described by the NLSE allowing direct quantitative comparison between theory and experiment [8].

Several problems pertaining to superfluidity and BEC can thus be studied in the framework of the NLSE. In this review, we concentrate on two such problems: (i) low-temperature superfluid turbulence [9–11] and (ii) stability of BEC in the presence of a moving obstacle [12–14] or an attractive interaction [15]. The paper is organized as follows: in section 2 the basic definitions and properties of the model of superflow are given. A short presentation of the hydrodynamic form, through Madelung's transformation, of NLSE with an arbitrary nonlinearity is derived. Simple solutions are discussed.

Section 3 is devoted to superfluid turbulence. The basic tools that are needed to numerically study 3D turbulence using NLSE are developed and validated in Section 3.1. The NLSE numerical results are given in section 3.2. Experimental

results are given in section 3.3.

The stability of BEC is studied in section 4. Exact 1D results are given in section 4.1 and a general formulation of stability is given in section 4.2. Numerical branch following methods are explained in section 4.3. The stability of a superflow around a cylinder is studied in section 4.4. The stability of an attractive Bose-Einstein condensate is studied in section 4.5. Finally, section 5 is our conclusion.

2 Hydrodynamics using the NLSE

The hydrodynamical form of NLSE with an arbitrary nonlinearity, corresponding to a barotropic fluid with an arbitrary equation of state is introduced in this section. Basic hydrodynamical features such that acoustic propagation and vortex time independent solutions are also discussed.

2.1 Madelung transformation

The most direct way to understand the generality of the connexion between the NLSE and fluid dynamics is to consider the following action [16] :

$$\mathcal{A} = 2\alpha \int dt \left\{ d^3x \left(\frac{i}{2} \left(\overline{\psi} \frac{\partial \psi}{\partial t} - \psi \frac{\partial \overline{\psi}}{\partial t} \right) \right) - \mathcal{F} \right\} \tag{1}$$

with

$$\mathcal{F} = \int d^3x \left(\alpha |\nabla \psi|^2 + f(|\psi|^2) \right) \tag{2}$$

where $\psi(\vec{x}, t)$ is a complex wave field and $\overline{\psi}$ its complex conjugate, α is a positive real constant and f is a polynomial in $|\psi|^2 \equiv \overline{\psi}\psi$ with real coefficients :

$$f(|\psi|^2) = -\Omega|\psi|^2 + \frac{\beta}{2}|\psi|^4 + f_3|\psi|^6 + \ldots + f_n|\psi|^{2n} \tag{3}$$

The NLSE is the Euler-Lagrange equation of motion for ψ corresponding to (1), it reads

$$\frac{\partial \psi}{\partial t} = -i \frac{\delta \mathcal{F}}{\delta \overline{\psi}},$$

or

$$\frac{\partial\psi}{\partial t} = i(\alpha\nabla^2\psi - \psi f'(|\psi|^2)) \tag{4}$$

Madelung's transformation [1,16]

$$\psi = \sqrt{\rho}\exp\left(i\frac{\varphi}{2\alpha}\right) \tag{5}$$

maps the nonlinear wave dynamics of ψ into equations of motion for a fluid of density ρ and velocity $\vec{v} = \nabla\varphi$. Indeed with the help of (5), (1) can be written

$$\mathcal{A} = -\int dtd^3x\left(\rho\frac{\partial\varphi}{\partial t} + \frac{1}{2}\rho(\nabla\varphi)^2 + 2\alpha f(\rho) + \frac{1}{2}(2\alpha\nabla(\sqrt{\rho}))^2\right) \tag{6}$$

and the corresponding Euler-Lagrange equations of motion read

$$\frac{\partial\rho}{\partial t} + \nabla\cdot(\rho\vec{v}) = 0 \tag{7}$$

$$\frac{\partial\varphi}{\partial t} + \frac{1}{2}(\nabla\varphi)^2 + 2\alpha f'(\rho) - 2\alpha^2\frac{\Delta\sqrt{\rho}}{\sqrt{\rho}} = 0 \tag{8}$$

Without the last term of (8) (the so-called "quantum pressure" term), these equations are the continuity and Bernoulli equations [4] for an isentropic, compressible, irrotational fluid.

It is possible to use this identification to define the corresponding "thermodynamical functions". Being isentropic ($S = 0$), the fluid is barotropic, and there is only one independent thermodynamical variable. First, the Bernoulli equation readily gives the fluid's enthalpy *per unit mass* as

$$h = 2\alpha f'(\rho). \tag{9}$$

Second, the $\frac{1}{2}\rho(\nabla\varphi)^2$ term of (6) corresponds to kinetic energy. Thus the fluid's internal energy *per unit mass* is given by

$$e = \frac{2\alpha f(\rho)}{\rho}. \tag{10}$$

The general thermodynamical identity

$$h = e + p/\rho, \tag{11}$$

gives the expression

$$p = 2\alpha(\rho f'(\rho) - f(\rho)) \tag{12}$$

for the fluid's pressure.

The physical dimensions of the variables used in (2) and (3) are fixed by the following considerations. Madelung's transformation (5) imposes that $[|\psi|^2] = [\rho] = M\,L^{-3}$ and $[\alpha] = L^2\,T^{-1}$. Using (10), one gets $[f(\rho)/\rho] = T^{-1}$ and thus, from (3), $[\Omega] = T^{-1}$, $[\beta] = T^{-1}\,\rho^{-1}$ and $[f_i] = T^{-1}\,\rho^{1-i}$. Note that, in the case of a Bose condensate of particles of mass m, α has the value $\hbar/2m$ [17].

2.2 Sound waves

2.2.1 Dispersion relation

The nature of the extra quantum pressure term in (8) can be understood through the dispersion relation corresponding to acoustic (density) waves propagating around a constant density level ρ_0. Setting $\rho = \rho_0 + \delta\rho$ (with $f'(\rho_0) = 0$), $\nabla\varphi = \delta u$ in (7) and in the gradient of (8), one gets (keeping only the linear terms) :

$$\begin{aligned} \partial_t \delta\rho + \rho_0 \nabla \delta u &= 0 \\ \partial_t \delta u + 2\alpha f''(\rho_0)\nabla\delta\rho - 2\alpha^2 \Delta \frac{\nabla\delta\rho}{2\rho_0} &= 0 \end{aligned}$$

or

$$\partial_t{}^2 \delta\rho = 2\alpha\rho_0 f''(\rho_0)\Delta\delta\rho - \alpha^2\Delta^2\delta\rho.$$

The dispersion relation for an acoustic wave $\delta\rho = \epsilon(\exp(i(\omega t - \vec{k}\cdot\vec{x})) + c.c.)$ (with $\epsilon \ll 1$) is thus

$$\omega = \sqrt{2\alpha\rho_0 f''(\rho_0)\vec{k}^2 + \alpha^2\vec{k}^4} \tag{13}$$

This relation shows that the quantum pressure has a dispersive effect that becomes important for large wave numbers. For small wavenumbers, one recovers the usual propagation, with a sound velocity given by

$$c = \left(\frac{\partial p}{\partial \rho}\right)^{\frac{1}{2}} = \sqrt{2\alpha\rho_0 f''(\rho_0)}.$$

The length scale $\xi = \sqrt{\alpha/(\rho_0 f''(\rho_0))}$ at which dispersion becomes noticeable is known as the "coherence length".

2.2.2 Nonlinear acoustics

The description given by linear acoustic can be somewhat improved by including the dominant nonlinear effects. Such an equation was derived in [18].

Numerical simulations of NLSE in one space dimension using a standard Fourier pseudo-spectral method [19] can be used to study the acoustic regime triggered by an initial disturbance of the form :

$$\psi(x) = 1 + ae^{-\frac{x^2}{l^2}}.$$

Such simulations were performed in ref. [18] where it was found that the shocks which would have appeared under compressible Euler dynamics (i.e. following Eq. (8) without the last term in r.h.s.) are regularized by the dispersion. There was no evidence of finite-time singularity in our numerics: the spectrum of the solution was well resolved, with a conspicuous exponential tail.

2.3 Vortices in 2 and 3D

Further insight on the connexion between the NLSE and fluid dynamics can be obtained by considering stationary solutions of the equations of motion. Indeed, by inspection of (1), time independent solutions of NLSE (4), are also solutions of the Real Ginzburg-Landau Equation (RGLE)

$$\frac{\partial \psi}{\partial t} = -\frac{\delta \mathcal{F}}{\delta \overline{\psi}} = (\alpha \nabla^2 \psi - \psi f'(|\psi|^2)). \tag{14}$$

They are thus extrema of the free energy $\mathcal{F}$.

The simplest solution of this type corresponds to a constant density fluid at rest. In this simple case, ψ is constant in space and (14) reads

$$f'(|\psi|^2) = -\Omega + \beta|\psi|^2 + 3f_3|\psi|^4 + \ldots + nf_n|\psi|^{2n-2} = 0. \tag{15}$$

This equation, for given values of the coefficients β and $f_i, i = 3, \ldots, n$ relates the fluid density $|\psi|^2$ to the value of Ω. Note that the Ω term of f does not play a crucial role in the NLSE dynamics. Indeed, it could be removed from the Bernoulli equation (8) by the change of variable $\varphi \to \varphi + 2\alpha\Omega t$ that amounts to a change of phase $\psi \to \psi e^{i\Omega t}$ in NLSE (4). It is however better, by convention, not to perform these changes of variable. With this convention, stationary solutions of (14) coincide with stationary solutions of (4). The Ω term of f is thus be fixed by the fluid's density through (15).

Another important type of time-independent solutions of NLSE are the vortex solutions. Madelung's transformation is singular when $\rho = 0$ (i.e. when both

$\Re(\psi) = 0$ and $\Im(\psi) = 0$. As two conditions are required, the singularities generically happen on points in two dimensions and lines in three dimensions. The circulation of $\vec{v}$ around such a generic singularity is $\pm 4\pi\alpha$. These topological defects are known in the context of superfluidity as "quantum vortices" [1]. Solutions of (14) with cylindrical symmetry can be obtained numerically [20]. The density profile of a vortex admits a horizontal asymptote near the core while the velocity diverges as the inverse of the core distance. The momentum density $\rho\vec{v}$ is thus a regular quantity. It is important to realize that such vortex solutions are *regular* solutions of the NLSE (4), the singularity stemming only from Madelung's transformation (5).

3 Superfluid turbulence

Superfluid flows (*i.e.* laboratory ^4He flows) are described mathematically in terms of Landau's two-fluid model [4]. When both normal fluid and superfluid vortices are present, their interaction, called "mutual friction", must be taken into account as pioneered by Schwarz [21]. At temperatures low enough for the normal fluid to be negligible (in practice below $T = 1^\circ K$ for helium at normal pressure), an alternative mathematical description is given by the Nonlinear Schrődinger Equation (NLSE), also called the Gross-Pitaevskii equation [2,3]. In this section, we will use the simplest form for f, corresponding to a cubic nonlinearity in the NLSE (4). The NLSE, with convenient normalization, reads

$$\partial_t \psi = ic/(\sqrt{2}\xi)(\psi - |\psi|^2\psi + \xi^2\nabla^2\psi). \tag{16}$$

Madelung's transformation (5) takes the form

$$\rho = |\psi|^2 \tag{17}$$

$$\rho v_j = ic\xi/\sqrt{2}(\psi\partial_j\overline{\psi} - \overline{\psi}\partial_j\psi) \tag{18}$$

where ξ is the so-called "coherence length" and c is the velocity of sound (when the mean density $\rho_0 = 1$ [1]). The superflow is irrotational, except near the nodal lines of ψ which are known to follow Eulerian dynamics [22,23]. These topological defects correspond to the superfluid vortices that appear naturally, with the correct velocity circulation, in this model [17].

The basic goal of the present section is to qualify the degree of analogy between turbulence in low–temperature superfluids and incompressible viscous fluids. We will do this by comparing numerical simulations of NLSE with existing numerical simulations of the Navier-Stokes equations, in particular the Taylor-Green (TG) vortex [24]. The TG vortex is the solution of the Navier-Stokes

equations with initial velocity field

$$\mathbf{v}^{TG} = \Big(\sin(x)\cos(y)\cos(z), -\cos(x)\sin(y)\cos(z), 0 \Big) \tag{19}$$

. This flow is well documented in the literature [25–27]. It admits symmetries that are used to speed up computations: rotation by π about the axis ($x = z = \pi/2$), ($y = z = \pi/2$) and ($x = y = \pi/2$) and reflection symmetry with respect to the planes $x = 0, \pi$, $y = 0, \pi$, $z = 0, \pi$. The velocity is parallel to these planes which form the sides of the *impermeable box* which confines the flow.

3.1 Tools for vortex dynamics

Under compressible fluid dynamics, an arbitrary chosen initial condition will generally lead to a regime dominated by acoustic radiation. In order to study vortex dynamics using NLSE, we thus need to prepare the initial data in such a way that the acoustic emission is as small as possible.

3.1.1 Preparation method

We now show how to construct a vortex array whose NLSE dynamics mimics the vortex dynamics of the large scale flow $\mathbf{v}^{TG}$. The first step of our method is based on a global Clebsch representation of $\mathbf{v}^{TG}$ and the second step minimizes the emission of acoustic waves [28].

The Clebsch potentials

$$\lambda(x,y,z) = \cos(x)\sqrt{2\,|\cos(z)|} \tag{20}$$

$$\mu(x,y,z) = \cos(y)\sqrt{2\,|\cos(z)|}\,\mathrm{sgn}(\cos(z)) \tag{21}$$

(where sgn gives the sign of its argument) correspond to the TG flow in the sense that $\nabla\times\mathbf{v}^{TG} = \nabla\lambda\times\nabla\mu$ and λ and μ are periodic functions of (x,y,z). These Clebsch potentials are used to map the physical space (x,y,z) into the (λ,μ) plane. The complex field ψ_c , corresponding to the large scale TG flow circulation, is given by $\psi_c(x,y,z) = (\psi_4(\lambda,\mu))^{[\gamma_d/4]}$ with $\gamma_d = 2\sqrt{2}/(\pi c\xi)$ ([ ] denotes the integer part of a real) and

$$\begin{aligned}\psi_4(\lambda,\mu) = \psi_e(\lambda - 1/\sqrt{2},\mu)\psi_e(\lambda,\mu - 1/\sqrt{2})\times \\ \psi_e(\lambda + 1/\sqrt{2},\mu)\psi_e(\lambda,\mu + 1/\sqrt{2})\end{aligned} \tag{22}$$

where $\psi_e(\lambda,\mu) = (\lambda + i\mu)\tanh(\sqrt{\lambda^2+\mu^2}/\sqrt{2}\xi)/\sqrt{\lambda^2+\mu^2}$.

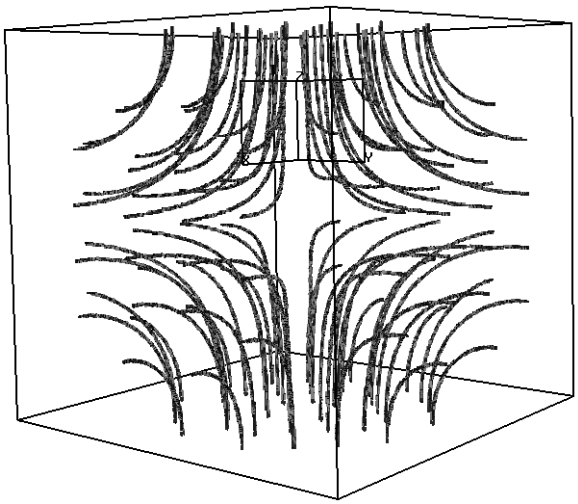

Fig. 1. Three-dimensional visualization of the vector field $\nabla \times (\rho \vec{v})$ for the Taylor-Green flow at time $t = 0$ with coherence length $\xi = 0.1/(8\sqrt{2})$, sound velocity $c = 2$ and $N = 512$ in the impermeable box $[0, \pi] \times [0, \pi] \times [0, \pi]$.

The second step of our procedure consists of integrating to convergence the Advective Real Ginzburg-Landau Equation (ARGLE):

$$\partial_t \psi = c/(\sqrt{2}\xi)(\psi - |\psi|^2\psi + \xi^2\nabla^2\psi) - i\mathbf{v}^{TG} \cdot \nabla\psi - (\mathbf{v}^{TG})^2/(2\sqrt{2}c\xi)\psi \tag{23}$$

with initial data $\psi = \psi_c$. It is shown in [9] that the TG symmetries can be used to expand $\psi(x, y, z, t)$, solution of the ARGLE and NLSE equations as:

$$\psi(x, y, z, t) = \sum_{m=0}^{N/2} \sum_{n=0}^{N/2} \sum_{p=0}^{N/2} \hat{\psi}(m, n, p, t) \cos mx \cos ny \cos pz \tag{24}$$

where N is the resolution and $\hat{\psi}(m, n, p, t) = 0$, unless m, n, p are either all even or all odd integers. Furthermore $\hat{\psi}(m, n, p, t)$ satisfies the additional conditions $\hat{\psi}(m, n, p, t) = (-1)^{r+1}\hat{\psi}(n, m, p, t)$ where $r = 1$ when m, n, p are all even and $r = 2$ when m, n, p are all odd. Implementing this expansion in a pseudo–spectral code yields a saving of a factor 64 in computational time and memory size when compared to general Fourier expansions.

The ARGLE converged periodic vortex array obtained in this manner is displayed on Fig. 1. with coherence length $\xi = 0.1/(8\sqrt{2})$, sound velocity $c = 2$ and resolution $N = 512$.

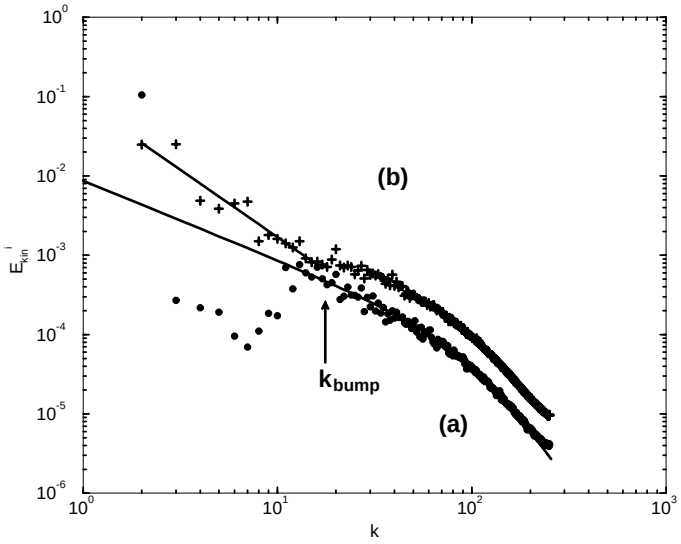

Fig. 2. Plot of the incompressible kinetic energy spectrum, $E^i_{kin}(k)$. The bottom curve (a) (circles) corresponds to time $t = 0$. The spectrum of a single axisymmetric 2D vortex multiplied by $(l/2\pi) = 175$ is shown as the bottom solid line. The top curve (b) (pluses) corresponds to time $t = 5.5$. A least-square fit over the interval $2 \leq k \leq 16$ with a power law $E^i_{kin}(k) = Ak^{-\ n}$ gives $n = 1.70$ (top solid line).

3.1.2 Energy spectra

The total energy of the vortex array, conserved by NLSE dynamics, can be decomposed into three parts $E_{tot} = 1/(2\pi)^3 \int d^3x(\mathcal{E}_{kin} + \mathcal{E}_{int} + \mathcal{E}_q)$, with kinetic energy $\mathcal{E}_{kin} = 1/2\rho v_j v_j$, internal energy $\mathcal{E}_{int} = (c^2/2)(\rho - 1)^2$ and quantum energy $\mathcal{E}_q = c^2\xi^2(\partial_j\sqrt{\rho})^2$. Each of these parts can be defined as the integral of the square of a field, for example, $\mathcal{E}_{kin} = 1/2(\sqrt{\rho}v_j)^2$. In order to separate the kinetic energy corresponding to compressibility effects, $\mathcal{E}_{kin}$ can be further decomposed into a compressible and incompressible parts using $\sqrt{\rho}v_j = (\sqrt{\rho}v_j)^c + (\sqrt{\rho}v_j)^i$ with $\nabla.(\sqrt{\rho}v_j)^i = 0$. Using Parseval's theorem, the angle-averaged kinetic energy spectrum is defined as:

$$E_{kin}(k) = \frac{1}{2}\int k^2 \sin\theta d\theta d\phi \left| \frac{1}{(2\pi)^3}\int d^3r e^{ir_j k_j}\sqrt{\rho}v_j \right|^2$$

which satisfies $E_{kin} = 1/(2\pi)^3 \int d^3x \mathcal{E}_{kin} = \int_0^\infty dk E_{kin}(k)$. The incompressible kinetic energy spectrum, $E^i_{kin}(k)$, is the angle-averaged spectrum computing over shells in Fourier space. A mode (m, n, p) belongs to the shell numbered as $k = [\sqrt{m^2 + n^2 + p^2} + 1/2]$.

The radius of curvature of the vortex lines in Fig. 1 is large compared to their radius. Thus these 3D lines can be considered as straight, and then compared to the 2D axisymmetric vortices which are exact solutions to the

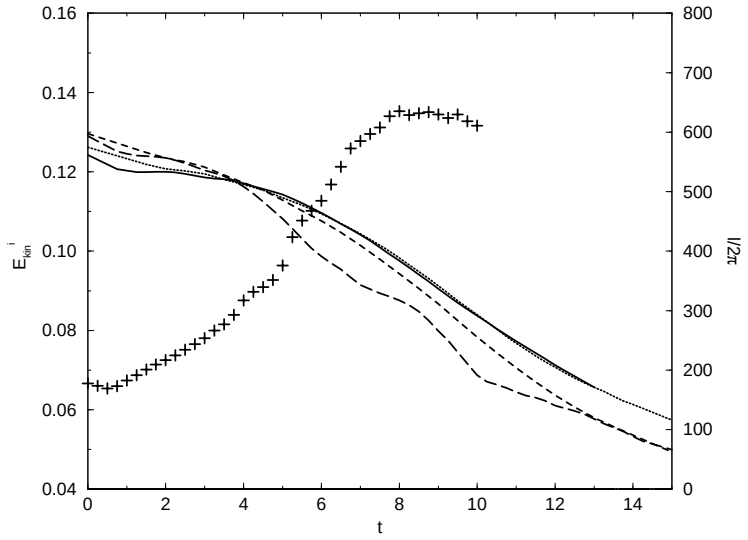

Fig. 3. Total incompressible kinetic energy, E^i_{kin}, plotted versus time for $\xi = 0.1/(2\sqrt{2})$, $N = 128$ (long–dash line); $\xi = 0.1/(4\sqrt{2})$, $N = 256$ (dash); $\xi = 0.1/(6.25\sqrt{2})$, $N = 400$ (dot) and $\xi = 0.1/(8\sqrt{2})$, $N = 512$ (solid line). All runs are realized with $c = 2$. The evolution of the total vortex filament length divided by 2π (crosses) for the $N = 512$ run is also shown (scale given on the right y-axis).

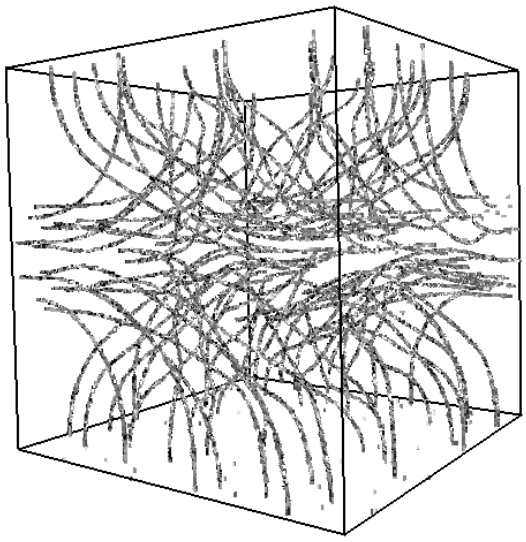

Fig. 4. Same visualization as in Fig. 1 but at time $t = 4$.

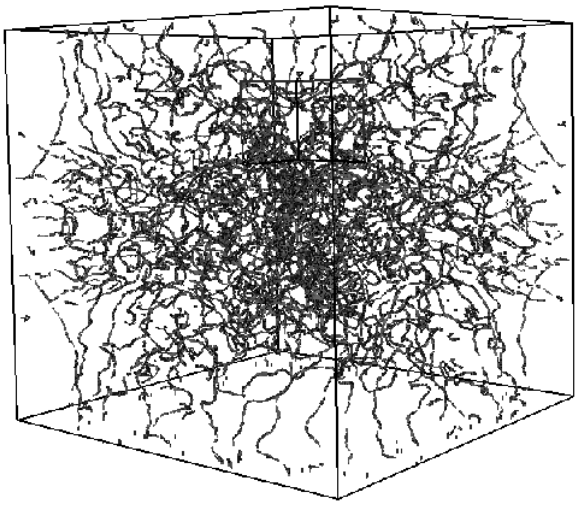

Fig. 5. Same visualization as in Fig. 1 but at time $t = 8$.

2D NLSE. A 2D vortex at the origin is given by $\psi^{vort}(r) = \sqrt{\rho(r)}\exp(im\varphi)$, $m = \pm 1$, where (r, φ) are polar coordinates. The vortex profile $\sqrt{\rho(r)} \sim r$ as $r \to 0$ and $\sqrt{\rho(r)} = 1 + O(r^{-2})$ for $r \to \infty$. It can be computed numerically using mapped Chebychev polynomials and an appropriate functional [9]. The corresponding velocity field is azimuthal and is given by $v(r) = \sqrt{2}c\xi/r$. Using the mapped Chebychev polynomials expansion for $\sqrt{\rho(r)}$, the angle averaged spectrum of $\sqrt{\rho}v_j$ can then be computed with the formula $E^{vort}_{kin}(k) = c^2\xi^2/(2\pi k)\left(\int_0^\infty dr J_0(kr)\partial_r\sqrt{\rho}\right)^2$ [9], where J_0 is the zeroth order Bessel function.

The incompressible kinetic energy spectrum E^i_{kin} of the ARGLE converged vortex array of Fig. 1 is displayed on Fig. 2. For large wavenumbers, the spectrum is well represented by extending a collection of 2D vortices into 3D vortex lines via $E^{line}_{kin}(k) \equiv const. \times E^{vort}_{kin}(k)$. (We will see that the constant of proportionality is related to the length l of vortex lines by $const. = l/(2\pi) = 175$ at time $t = 0$.) In contrast, the small wavenumber region cannot be represented by E^{line}_{kin}. This stems from the average separation distance between the vortex lines in Fig. 1. Calling this distance $d_{bump} = k^{-1}_{bump} = 1/16$, the wavenumber range between the large-scale wavenumber $k = 2$ and the characteristic separation wavenumber k_{bump} can be explained by interference effects. Due to constructive interference, the energy spectrum at $k = 2$ has a value close to its corresponding value in TG viscous flow (namely 0.125), which is much above the value of $E^{line}_{kin}(k = 2)$. In contrast, for $2 < k \leq k_{bump}$, destructive interference decreases E^i_{kin} below E^{line}_{kin}.

3.2 Numerical results

The evolution in time via NLSE (16) of the incompressible kinetic energy is shown in Fig. 3. The main quantitative result is the remarkable agreement of the energy dissipation rate, $-dE^i_{kin}/dt$, with the corresponding data in the incompressible viscous TG flow (see reference [25], and reference [29], figure 5.12). Both the moment $t_{max} \sim 5 - 10$ of maximum energy dissipation (the inflection point of Fig. 3) and its value $\epsilon(t_{max}) \sim 10^{-2}$ at that moment are in quantitative agreement. Furthermore, both t_{max} and $\epsilon(t_{max})$ depend weakly on ξ.

Another important quantity studied in viscous decaying turbulence is the scaling of the kinetic energy spectrum during time evolution and, especially, at the moment of maximum energy dissipation, where a $k^{-5/3}$ range can be observed (see reference [25]). Fig. 2 (b) shows the energy spectrum at $t = 5.5$. A least-square fit over the interval $2 \leq k \leq 16$ with a power law $E^i_{kin}(k) = Ak^{-\ n}$ gives $n = 1.70$ (solid line). For $5 < t < 8$, a similar fit gives $n = 1.6 \pm 0.2$ (data not shown). Fitting $E^i_{kin}(k)$ in the interval $30 \leq k \leq 170$ with $l/(2\pi)$ times $E^{vort}_{kin}(k)$ leads to $l/2\pi = 452$, roughly three times the $t = 0$ length of the vortex lines. The time evolution of $l/2\pi$ obtained by this procedure is displayed in Fig. 3, showing that the length continues to increase beyond t_{max}. The computations were performed with $c = 2$ corresponding to a *root-mean-square* Mach number $M_{rms} \equiv |\mathbf{v}^{TG}_{rms}|/c = 0.25$. As it is very costly to decrease M_{rms}, we checked [9] that compressible effects were non-dominant at this value of M_{rms}.

The vortex lines are visualized in physical space in Figs. 4 and 5 at time $t = 4$ and $t = 8$. At $t = 4$, no reconnection has yet taken place while a complex vortex tangle is present at $t = 8$. Detailed visualizations (data not shown) demonstrate that reconnection occurs for $t > 5$. Note that the viscous TG vortex also undergoes a qualitative (and quantitative) change in vortex dynamics around $t \sim 5$.

3.3 Experimental results

The TG flow is related to an experimentally studied swirling flow [30–32]. The relation between the experimental flow and the TG vortex is a similarity in overall geometry [30]: a shear layer between two counter–rotating eddies. The TG vortex, however, is periodic with free-slip boundaries while the experimental flow is contained inside a tank between two counter–rotating disks.

The spectral behavior of NLSE can be compared to standard (viscous) turbulence only for $k \leq k_{bump}$. It is thus of interest to estimate the scaling of k_{bump}

in terms of the characteristic parameters of the large scale flow and of the fluid. As seen above, $k_{bump} \sim d_{bump}^{-1}$, where d_{bump} is the average distance between neighboring vortices. Consider a flow with characteristic integral scale l_0 and large scale velocity u_0 (in the case of the TG flow, $l_0 \sim 1$ and $u_0 \sim 1$). The fluid characteristics are the velocity of sound c and the coherence length ξ (with corresponding wavenumber $k_\xi \sim \xi^{-1}$). The number n_d of vortex lines crossing a typical large–scale l_0^2 area is given by the ratio of the large–scale flow circulation $l_0 u_0$ to the quantum of circulation $\Gamma = 4\pi c\xi/\sqrt{2}$, i.e $n_d \sim l_0 u_0/c\xi$. On the other hand, the assumption that the vortices are uniformly spread over the large scale area gives $n_d \sim l_0^2/d_{bump}^2$. Equating these two evaluations of n_d yields the relation $d_{bump} \sim l_0\sqrt{(c\xi)/(l_0 u_0)}$.

In the case of helium, the viscosity at the critical point ($T = 5.174°K$, $P = 2.2\ 10^5\ Pa$) is $\nu_{cp} = 0.27 \times 10^{-7} m^2 s^{-1}$ while the quantum of circulation, $\Gamma = h/m_{He}$ has the value $0.99 \times 10^{-7} m^2 s^{-1}$. Thus, $0.25\nu_{cp} \sim \Gamma$. The order of magnitude for d_{bump} is thus $d_{bump} = l_0/\sqrt{R_{cp}} \sim l_\lambda$ where R_{cp} is the integral scale Reynolds number at the critical point and l_λ the Taylor micro-scale. In other words, the value of d_{bump} in a superfluid helium experiment at $T = 1°K$ is of the same order as the Taylor micro-scale in the same experimental set-up run with viscous helium at the critical point.

The experimental set-up is similar to the one described in [31]. Some modifications have been made to work down to $1.2K$. The flow is produced in a cylinder, 8 cm in diameter and 12 cm high, limited axially by two counter-rotating disks. One disk is flat and, on the other one, are fixed 8 radial blades, forming an angle of 45^o between each other. A stator is mounted at half the total height of the cell in order to stabilize the turbulent shear region. The two disks are driven by two DC motors rotating from 1 to 30 Hz. The whole system is enclosed directly in a liquid Helium bath which is used as the experimental fluid, the main difference with the set-up described in [31]. The temperature of the fluid is fixed by the pressure above the liquid bath, which is itself controlled by the pumping system.

Local pressure fluctuations are measured by using small total-head pressure tubes, immersed in the flow. The pressure sensors are hollow metallic tubes, connected to a quartz pressure transducer WHM 112 A22 from PCB. Details are given in [11].

In normal fluids, the pressure measured at the tip of the total-head tube can be related to the upstream flow $U(t)$ and the local pressure $P(t)$ using Bernoulli theorem:

$$P_{\text{meas}}(t) = P(t) + \rho U^2(t)/2 \tag{25}$$

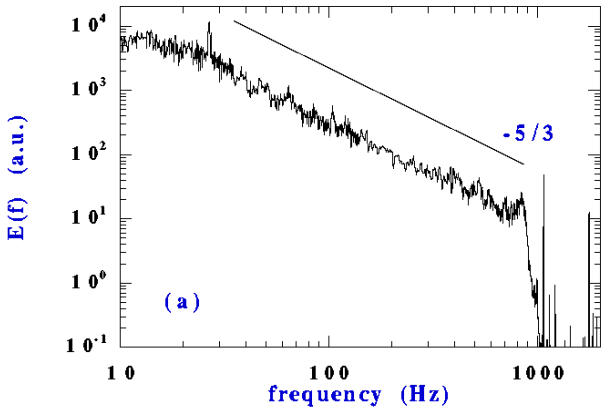

Fig. 6. Experimental pressure fluctuation spectrum (in non-dimensional units) measured with a total head pressure tube immersed in the flow at $T = 2.3\ K$.

In the flow region where the probe is immersed, a well established axial mean flow U exists so that, after removing the mean parts of Equation (1), one gets:

$$p_{\text{meas}}(t) = p(t) + \rho U u(t) \tag{26}$$

where p_{meas}, p and u are the fluctuations of the measured pressure, the actual pressure, and the local velocity respectively. It is currently admitted that, in ordinary turbulent situations, and at low fluctuation rates, Equation (2) is dominated by the dynamic term, so that, by measuring the pressure fluctuations at the total head tube, one has a direct access to the velocity fluctuations $u(t)$.

The situation is less clear when the probe is immersed in the superfluid. It is however possible to write an equation similar to (2). Details can be found in [11].

The analysis of the pressure fluctuations obtained with the total head tube placed at 2 cm above the mid plane and 2 cm from the cylinder axis, yields interesting informations. Figures 6 and 7 shows the spectra of the pressure fluctuations above and below T_λ (i.e respectively at $2.3K$ and $1.4K$). Fig. 6 clearly shows, as expected, that such fluctuations follow a Kolmogorov regime between the injection scale (signaled by the peak at 25 Hz) and the largest resolved frequency, i.e 900 Hz. The spectrum obtained at $1.4K$ is similar to that obtained at $T = 2.3K$ (see Fig. 7). A clear Kolmogorov like regime exists for the same range of frequencies. The corresponding Kolmogorov constant turns out also to be indistinguishable from the classical value. We have further analyzed the deviations from Kolmogorov in the superfluid regime. The

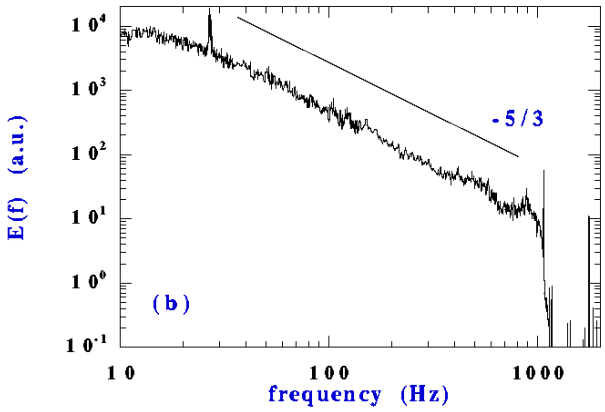

Fig. 7. Experimental pressure fluctuation spectrum (in non-dimensional units) measured with a total head pressure tube immersed in the flow at $T = 1.4\ K$.

striking result is that they have the same magnitude as in classical turbulence. More details are given in [33].

These observations - both on global and local quantities - agree pretty well the theoretical approach developed in the previous section. In particular, it seems rather clear that Kolmogorov cascade survives in the superfluid regime.

4 Stability of stationary solutions

This section is devoted to the stability of BEC. Exact 1D bifurcation results are given in section 4.1. A general formulation of stability is given in section 4.2. Numerical branch following methods are explained in section 4.3. The stability of a superflow around a cylinder is studied in section 4.4 and attractive Bose-Einstein condensates are studied in section 4.5.

4.1 Exact solution in 1D

4.1.1 Definition of the system

We consider a punctual impurity moving within a 1D superflow. In the frame of the moving impurity, the system can be described by the following action

functional

$$\mathcal{A}[\psi,\overline{\psi}] = \int \mathrm{d}t \left[\frac{i}{2}\int \mathrm{d}x\,(\overline{\psi}\partial_t\psi - \psi\partial_t\overline{\psi}) - \mathcal{K}\right]. \tag{27}$$

In this expression, ψ is a complex field, $\overline{\psi}$ its conjugate and the energy functional $\mathcal{K}$ reads

$$\mathcal{K} = \mathcal{E} - v\mathcal{P} + v\left[R^2(+\infty)\phi(+\infty) - R^2(-\infty)\phi(-\infty)\right], \tag{28}$$

with

$$\mathcal{E} = \int \mathrm{d}x\,\left[|\partial_x\psi|^2 + \frac{1}{2}(|\psi|^2-1)^2 + g\delta(x)(|\psi|^2-1)\right], \tag{29}$$

$$\mathcal{P} = \int \mathrm{d}x\,\frac{1}{2i}\left[\overline{\psi}(\partial_x\psi) - \psi(\partial_x\overline{\psi})\right], \tag{30}$$

$$\psi = R\exp(i\phi)\,. \tag{31}$$

The Dirac (pseudo) potential $g\delta(x)$ in (29) represents the impurity and the last term in (28) imposes the appropriate boundary conditions for the phase ϕ [34]. R obeys the boundary conditions $R^2(\pm\infty) = 1$.

The Euler-Lagrange equation associated to (27), $\delta\mathcal{A}/\delta\overline{\psi} = 0$, is the nonlinear Schrödinger equation (NLSE)

$$i\partial_t\psi = -\partial_{xx}\psi + iv\,\partial_x\psi - \psi + |\psi|^2\psi + g\delta(x)\psi\,, \tag{32}$$

where the discontinuity condition

$$\partial_x\psi(0^+,t) - \partial_x\psi(0^-,t) = g\psi(0,t) \tag{33}$$

is imposed in order to balance the $g\delta(x)\psi$ singularity with the $-\partial_{xx}\psi$ term for all times t.

4.1.2 Stationary solutions

Time-independent solutions of the NLSE (32) are best studied by performing the change of variables defined above in (31): $\psi = R\exp(i\phi)$. Using these variables, the NLSE reads

$$\partial_t R = v\partial_x R - R\partial_{xx}\phi - 2\partial_x R\partial_x\phi\,, \tag{34}$$

$$\partial_t\phi = v\partial_x\phi - (\partial_x\phi)^2 + 1 - R^2 - g\delta(x) + \frac{\partial_{xx}R}{R}\,, \tag{35}$$

and the jump condition (33) reads

$$\partial_x R(0^+,t) - \partial_x R(0^-,t) = gR(0,t)\,, \tag{36}$$

$$\partial_x\phi(0^+,t) - \partial_x\phi(0^-,t) = 0\,. \tag{37}$$

Note that Eqs. (34) and (35) can be respectively interpreted as the continuity and Bernoulli equations for a fluid of density $\rho = R^2(x)$ and velocity $u = 2\partial_x\phi$ (as done in section 2).

Explicit time-independent solutions of Eqs. (34) and (35) were found by Hakim[34], using the so-called gray solitons (a nonlinear optics terminology). Gray solitons [35,36] are stationary solutions of Eqs. (34) and (35), *without* the potential term $g\delta(x)$. They are localized density depletion of the form

$$R^2_{\rm GS}(x) = v^2/2 + (1 - v^2/2)\tanh^2[\sqrt{1/2 - v^2/4}\, x]\,, \tag{38}$$

$$\phi_{\rm GS}(x) = \arctan\left(\frac{v\sqrt{2 - v^2}}{\exp[\sqrt{2 - v^2}\, x] + v^2 - 1}\right). \tag{39}$$

Patching together pieces of gray solitons, Hakim found the following ξ-indexed stationary solutions of Eqs. (34) and (35), *including* the potential term $g\delta(x)$

$$R_\xi(x) = R_{\rm GS}(x \pm \xi)\,, \qquad x \gtrless 0 \tag{40}$$

$$\phi_\xi(x) = \phi_{\rm GS}(x \pm \xi) - \phi_{\rm GS}(\pm\xi)\,, \qquad x \gtrless 0 \tag{41}$$

where the jump conditions (36) and (37) impose the relation

$$g(\xi) = \sqrt{2}(1 - v^2/2)^{3/2}\frac{\tanh[\sqrt{1/2 - v^2/4}\,\xi]}{v^2/2 + \sinh^2[\sqrt{1/2 - v^2/4}\,\xi]}\,. \tag{42}$$

The function $g(\xi)$ reaches a maximum $g_c = g(\xi_c)$ at $\xi_c = \frac{\mathrm{argcosh}(\frac{1+\sqrt{1+4v^2}}{2}}{\sqrt{2-v^2}}$ with

$$g_c = 4(1 - v^2/2)\frac{[\sqrt{1 + 4v^2} - (1 + v^2)]^{1/2}}{2v^2 - 1 + \sqrt{1 + 4v^2}}\,. \tag{43}$$

The two stationary solutions of (32) corresponding to $\xi_+(g) > \xi_c$ and $\xi_-(g) < \xi_c$ obtained by inverting (42) for $g < g_c$ thus disappear, merging in a saddle-node bifurcation at a critical strength g_c. Note that the bifurcation can also be obtained by varying v and keeping g constant. In the following, the strength g of the delta function is used as the control parameter of our system, keeping v constant.

The bifurcation diagram corresponding to the energy $\mathcal{K}$ (see Eq. (28)) is shown on fig.8. The energetically unstable and stable solutions ($\mathcal{K}(\xi_-(g)) > \mathcal{K}(\xi_+(g))$) are also displayed on the figure. Note that the phase $\phi_\xi(x)$, as defined in eq. (41), differs from that considered in [34] by an (x-independent) constant. The phase in [34] is set to 0 at $x = +\infty$, whereas (41) is antisymmetric in x. This difference is unimportant because Eqs. (34) and (35) are invariant under the constant phase shift

$$\phi(x) \mapsto \phi(x) + \varphi\,. \tag{44}$$

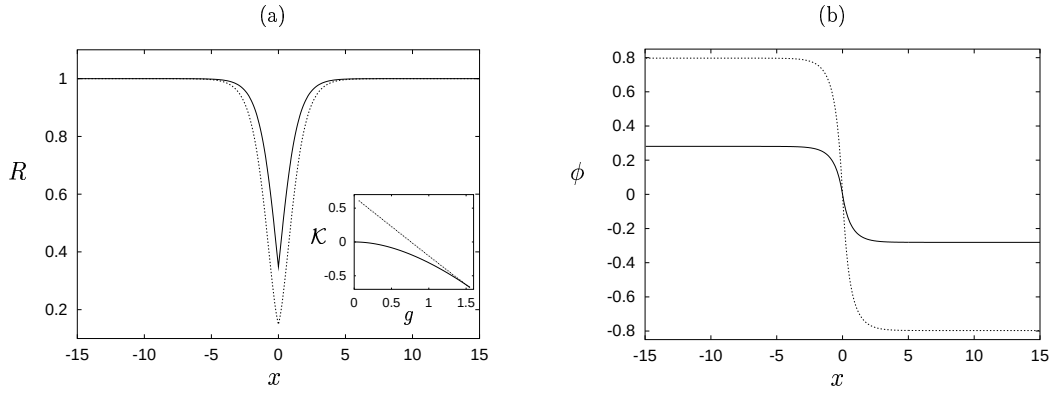

Fig. 8. (a) Modulus R of the stable (—) and unstable (- - -) stationary solutions of eq.(32) (see eq.(40)) for $g = 1.250$ and $v = 0.5$; insert, energy functional $\mathcal{K}$ of the stationary solutions versus g for $v = 0.5$ (see eq.(28)); lower branch: energetically stable branch, upper branch: energetically unstable branch. The bifurcation occurs at $g = 1.5514$ (b) Phase ϕ of the stable (—) and unstable (- - -) stationary solutions (see eq.(41)), same conditions as in (a).

4.2 General formulation

In this section we define and test the numerical tools needed to obtain the stationary solutions of the NLSE.

Consider the following action functional associated to the NLSE

$$\mathcal{A} = \int d\tilde{t} \left\{ \int d\tilde{\mathbf{x}} \frac{i}{2} \left(\overline{\psi} \frac{\partial \psi}{\partial \tilde{t}} - \psi \frac{\partial \overline{\psi}}{\partial \tilde{t}} \right) - \mathcal{F} \right\}, \tag{45}$$

where ψ is a complex field, $\overline{\psi}$ its conjugate and $\mathcal{F}$ is the energy of the system. Here, $\mathbf{x}$ and $\tilde{t}$ correspond to adequately nondimensionalized space and time variables respectively.

The Euler-Lagrange equation corresponding to (45) leads to the NLSE in terms of the functional $\mathcal{F}$

$$\frac{\partial \psi}{\partial \tilde{t}} = -i \frac{\delta \mathcal{F}}{\delta \overline{\psi}}. \tag{46}$$

This equation obviously admits ψ_S as a stationary solutions if $\delta\mathcal{F}/\delta\psi|_{\psi=\psi_S} = 0$. Thus, stationary solutions of (46) are extrema of $\mathcal{F}$. In general, we are looking for an extremum of an energy functional $\mathcal{E}$ under some constraint $\mathcal{Q}[\psi] = \mathrm{c}st$. The usual Lagrange multiplier trick consists in introducing a control parameter ν and, rather than solving for extrema of $\mathcal{E}[\psi]$, searching for extrema of the new functional $\mathcal{F}[\psi] = \mathcal{E}[\psi] - \nu\mathcal{Q}[\psi]$. We thus solve for

$$\left. \frac{\delta \mathcal{F}}{\delta \psi} \right|_{\nu=\mathrm{cst.}} = 0. \tag{47}$$

We now turn to the precise definitions, corresponding to the two systems considered in this section : (a) Bose-Einstein Condensates and (b) Superflows.

4.2.1 Superflows

In the problem of a superflow past an obstacle, $\mathcal{E}$ is the hydrodynamic energy and $\nu \equiv \vec{U}$ is the flow velocity with respect to the obstacle [12,14]. This implies that $\mathcal{Q} \equiv \vec{\mathcal{P}}$ is the flow momentum. Functionals $\mathcal{F}$, $\mathcal{E}$ and $\vec{\mathcal{P}}$ are given by the expressions

$$\mathcal{F} = \mathcal{E} - \vec{\mathcal{P}} \cdot \vec{U} \tag{48}$$

$$\mathcal{E} = c^2 \int d^3x \left([-1 + V(\vec{x})]|\psi|^2 + \frac{1}{2}|\psi|^4 + \xi^2 |\nabla\psi|^2 \right) \tag{49}$$

$$\vec{\mathcal{P}} = \sqrt{2} c\xi \int d^3x \frac{i}{2} \left(\psi \nabla\overline{\psi} - \overline{\psi}\nabla\psi \right). \tag{50}$$

Here, c and ξ are the physical parameters characterizing the superfluid. They correspond to the speed of sound (c) for a fluid with mean density $\rho_0 = 1$, and to the coherence length (ξ). The potential $V(\vec{x})$ is used to represent a cylindrical obstacle of diameter D. The NLSE reads

$$\frac{\partial\psi}{\partial t} = -\frac{i}{\sqrt{2}c\xi} \frac{\delta\mathcal{F}}{\delta\overline{\psi}} = i\frac{c}{\sqrt{2}\xi} \left([1 - V(\vec{x})]\psi - |\psi|^2\psi + \xi^2\nabla^2\psi \right) + \vec{U} \cdot \nabla\psi. \tag{51}$$

We will be interested in the solutions of $\delta\mathcal{F}/\delta\overline{\psi} = 0$, for a given value of $\vec{U}$. According to equation (47), these solutions are extrema of $\mathcal{E}$ at constant momentum $\vec{\mathcal{P}}$.

4.2.2 Bose-Einstein Condensates

We consider a condensate of $\mathcal{N}$ particles of mass m and effective scattering length a in a radial confining harmonic potential $V(r) = m\omega^2 r^2/2$ [15]. Quantities are rescaled by the natural quantum harmonic oscillator units of time $\tau_0 = 1/\omega$ and length $L_0 = \sqrt{\hbar/m\omega}$, thus obtaining the nondimensionalized variables $\tilde{t} = t/\tau_0$, $\tilde{\mathbf{x}} = \mathbf{x}/L_0$ and $\tilde{a} = 4\pi a/L_0$. The control parameter ν becomes in this context the chemical potential μ. The total number of particles in the condensate is therefore given by $\mathcal{Q} \equiv \mathcal{N}$. Functionals $\mathcal{F}$, $\mathcal{E}$ and $\mathcal{N}$ are given, in terms of rescaled variables, by

$$\mathcal{F} = \mathcal{E} - \mu\mathcal{N} \tag{52}$$

$$\mathcal{E} = \int d^3\tilde{\mathbf{x}} \left(\frac{1}{2}|\nabla_{\tilde{\mathbf{x}}}\psi|^2 + V(\tilde{\mathbf{x}})|\psi|^2 + \frac{\tilde{a}}{2}|\psi|^4 \right) \tag{53}$$

$$\mathcal{N} = \int d^3\tilde{\mathbf{x}}|\psi|^2. \tag{54}$$

Two different situations are possible, depending on the sign of the (rescaled) effective scattering length $\tilde{a}$. When $\tilde{a}$ is positive the particles interact repulsively. A negative $\tilde{a}$ corresponds to an attractive interaction. The dynamical equation is

$$\frac{\partial\psi}{\partial\tilde{t}} = -i\frac{\delta\mathcal{F}}{\delta\overline{\psi}} = i\left[\frac{1}{2}\nabla^2_{\tilde{\mathbf{x}}}\psi - \frac{1}{2}|\tilde{\mathbf{x}}|^2\psi - \left(\tilde{a}|\psi|^2 - \mu\right)\psi\right]. \tag{55}$$

We will be interested in the solutions of $\delta\mathcal{F}/\delta\overline{\psi} = 0$, for a given value of μ. According to equation (47), these solutions are extrema of $\mathcal{E}$ at constant particle number $\mathcal{N}$.

4.3 Branch following methods

When the extremum of $\mathcal{F}$ is a local *minimum*, the stationary solution ψ_S of (51) can be reached by a relaxation method. If the extremum is not a minimum, Newton's iterative method is used to solve for ψ_S.

4.3.1 Relaxation method

In what remains of this section, we will write the NLSE under the following generic form, which is valid for both the Bose-Einstein condensates and the superflow past an obstacle:

$$\frac{\partial\psi}{\partial t} = -i\frac{\delta\mathcal{F}}{\delta\overline{\psi}} = i\left(\alpha\nabla^2\psi + \left[\Omega - V(\vec{x})\right]\psi - \beta|\psi|^2\psi\right) + \vec{U}\cdot\nabla\psi. \tag{56}$$

When the extremum of $\mathcal{F}$ is a local *minimum*, the stationary solution ψ_S of (56) can be reached by integrating to relaxation the associated real Ginzburg-Landau equation (RGLE)

$$\frac{\partial\psi}{\partial t} = -\frac{\delta\mathcal{F}}{\delta\overline{\psi}} = \alpha\nabla^2\psi + \left[\Omega - V(\vec{x})\right]\psi - \beta|\psi|^2\psi - i\vec{U}\cdot\nabla\psi. \tag{57}$$

Indeed, (56) and (57) have the same stationary solutions.

In our numerical computations, equation (57) is integrated to convergence by

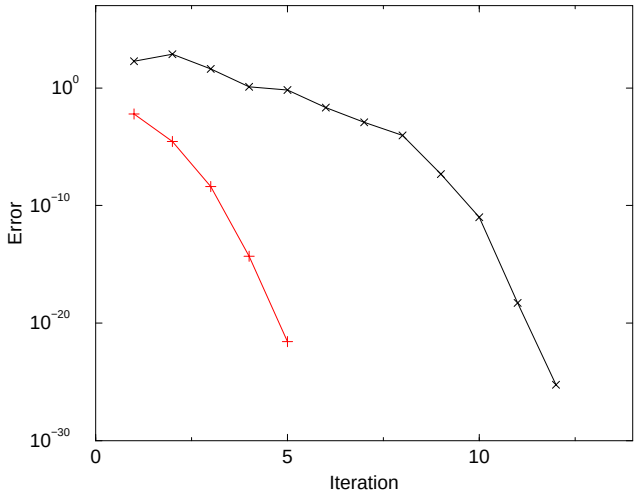

Fig. 9. Two typical examples of the Newton method convergence towards the solution of equation (60) for the problem of a superflow past a cylinder with $\xi/D = 1/10$ and a field $\psi_{(j)}$ discretized into $n = 128 \times 64 = 8190$ collocation points. The error measure is given by $\sum_{j=1}^{n} f_{(j)}^2(\psi)/n$. The convergence is faster than exponential, as expected for a Newton method.

using the Forward-Euler/Backwards-Euler time stepping scheme

$$\psi(t+\sigma) = \Theta^{-1}\left[\left(1 - i\,\sigma\,\vec{U}\cdot\nabla\right) + \sigma\,\left([\Omega - V(\vec{x})] - \beta|\psi(t)|^2\right)\right]\psi(t) \quad (58)$$

with

$$\Theta = \left[1 - \sigma\,\alpha\nabla^2\right]. \quad (59)$$

The advantage of this method is that it converges to the stationary solution of (56) independently of the time step σ.

4.3.2 Newton method

We use Newton's method [37] to find unstable stationary solutions of the RGLE.

In order to work with a well-conditioned system [38], we search for the fixed points of (58). These can be found as the roots of

$$f(\psi) = \Theta^{-1}\left[\left(1 - i\,\sigma\,\vec{U}\cdot\nabla\right) + \sigma\,\left([\Omega - V(\vec{x})] - \beta|\psi(t)|^2\right)\right]\psi(t) - \psi(t), \quad (60)$$

where Θ^{-1} was already introduced in equation (58). Calling $\psi_{(j)}$ the value of the field ψ over the j-th collocation point, finding the roots of $f(\psi)$ is equivalent iterating the Newton step

$$\psi_{(j)} = \psi_{(j)} + \delta\psi_{(j)} \quad (61)$$

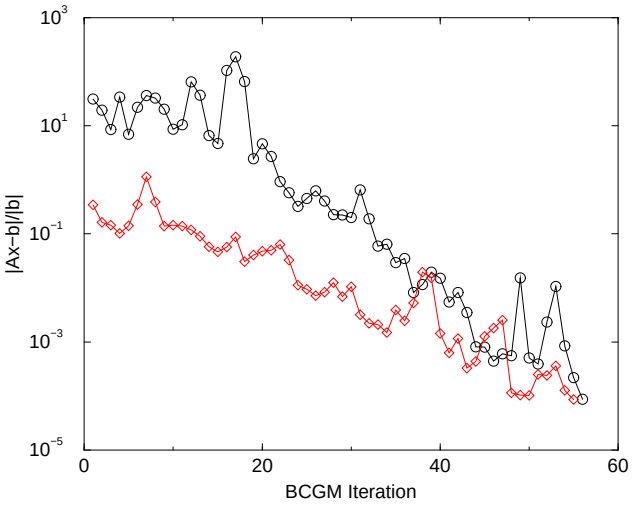

Fig. 10. Two typical examples of a bi-conjugate gradient method convergence corresponding to the case shown on figure 9. The convergence of the relative error achieved for the **x** solution of **Ax=b** is given by $|\mathbf{Ax\text{-}b}|/|\mathbf{b}|$, where $\mathbf{A}=[df_{(j)}/d\psi_{(k)}]$, $\mathbf{b}=-f_{(j)}(\psi)$ and $\mathbf{x}=\delta\psi_{(k)}$.

up to convergence. Every Newton step (61) requires the solution for $\delta\psi_{(k)}$ of

$$\sum_k \left[\frac{df_{(j)}}{d\psi_{(k)}}\right] \delta\psi_{(k)} = -f_{(j)}(\psi). \tag{62}$$

This solution is obtained by an iterative bi-conjugate gradient method (BCGM) [39]. The BCGM uses the direct application of $[df_{(j)}/d\psi_{(k)}]$ over an arbitrary field φ to obtain an approximative solution of (62). Note that since the convergence of the time step (58) does not depend on σ, the roots found through this Newton iteration are also independent of σ. Therefore, σ becomes a free parameter that can be used to adjust the pre-conditioning of the system in order to optimize the convergence of the BCGM [38].

4.3.3 Implementation

We use standard Fourier pseudo spectral methods [19]. Typical convergences of the Newton and bi-conjugate gradient iterations are shown in figures 9 and 10.

In the case of the radially symmetric Bose Condensate, $\psi(r,\tilde{t})$ is expanded as $\psi(r,\tilde{t}) = \sum_{n=0}^{N_R/2} \hat{\psi}_{2n}(\tilde{t}) T_{2n}(r/R)$, where T_n is the n-th order Chebychev polynomial and $\hat{\psi}_{N_R}$ is fixed to satisfy the boundary condition $\psi(R,\tilde{t})=0$.

The time integration of the NLSE is done by using a fractional step (Operator-Splitting) method [40].

4.4 Stability of 2D superflow around a cylinder

In this section, following references [12–14], we investigate the stationary stable and unstable (nucleation) solutions of the NLSE describing the superflow around a cylinder, using the numerical methods developed in section 4.3. We study a disc of diameter D, moving at speed $\vec{U}$ in a two-dimensional (2D) superfluid at rest. The NLSE (51) can be mapped into two hydrodynamical equations by applying Madelung's transformation [1,16]:

$$\psi = \sqrt{\rho}\exp\left(\frac{i\phi}{\sqrt{2}c\xi}\right). \tag{63}$$

The real and imaginary parts of the NLSE produce for a fluid of density ρ and velocity

$$\vec{v} = \nabla\phi - \vec{U}, \tag{64}$$

the following equations of motion

$$\frac{\partial\rho}{\partial t} + \nabla\left(\rho\vec{v}\right) = 0 \tag{65}$$

$$\left[\frac{\partial\phi}{\partial t} - \vec{U}\cdot\nabla\phi\right] + \frac{1}{2}(\nabla\phi)^2 + c^2[\rho - \Omega(\vec{x})] - c^2\xi^2\frac{\nabla^2\sqrt{\rho}}{\sqrt{\rho}} = 0. \tag{66}$$

In the coordinate system $\vec{x}$ that follows the obstacle, these equations correspond to the continuity equation and to the Bernoulli equation [4] (with a supplementary *quantum pressure* term $c^2\xi^2\nabla^2\sqrt{\rho}/\sqrt{\rho}$) for an isentropic, compressible and irrotational flow. Note that, in the limit where $\xi/D \to 0$, the quantum pressure term vanishes and we recover the system of equations describing an Eulerian flow.

4.4.1 Bifurcation diagram and scaling in 2D

In this section, varying the ratio of the coherence length ξ to the cylinder diameter D, we obtain scaling laws in the $\xi/D \to 0$ limit.

Bifurcation diagram

We present results for $\xi/D = 1/10$ which are representative of all ratios we computed. The functional $\mathcal{E}$ and energy $\mathcal{F}$ of the stationary solutions are shown in Fig. 11 as a function of the Mach number ($M = |\vec{U}|/c$). The stable branch (a) disappears with the unstable solution (c) at a saddle-node bifurcation when $M = M^c \approx 0.4286$. The energy $\mathcal{F}$ has a cusp at the bifurcation

point, which is the generic behavior for a saddle-node. There are no stationary solutions beyond this point. When $M \approx 0.4282$, the unstable symmetric branch (c) bifurcates at a pitchfork to a pair of asymmetric branches (b). Their nucleation energy barrier is given by $(\mathcal{F}_{b'} - \mathcal{F}_{a'})$ which is roughly half of the barrier for the symmetric branch $(\mathcal{F}_{c'} - \mathcal{F}_{a'})$.

We can relate branches in Fig. 11 to the presence vortices in the solution. When $M^{\rm pf} \leq M \leq M^c$, solutions are irrotational ($M^{\rm pf} \sim 0.405$ as indicated in Fig. 11). For $M \leq M^{\rm pf}$ the stable branch (a) remains irrotational (Fig. 12A) while the unstable branch (b) corresponds to a one vortex solution (Fig. 12B) and the unstable branch (c), to a two vortex solution (Fig. 12C). The distance between the vortices and the obstacle in branches (b) and (c) increases when M is decreased. Branch (c) is precisely the situation described in [41]. Furthermore, the value $M^c \approx 0.4286$ is close to the predicted value $\sqrt{2/11}$. Figure 12D shows the result of integrating the NLSE forward in time with, as initial condition, a slightly perturbed unstable symmetric stationary state (Fig. 12C). The perturbation drives the system over the nucleation barrier and cycles it, after the emission of two vortices, back to a stationary stable solution. This shows that the branch (c) corresponds to hyperbolic fixed points of NLSE.

Figures 12E,F show the phase of the field at the surface of the disc ($r = D/2$ and $\theta \in [0, 2\pi]$) for four different flow speeds. In both unstable branches, 2π-discontinuities, a diagnostic of vortex crossing, appear between $M = 0.40$ and $M = 0.41$.

Scaling laws

We now characterize the dependence on ξ/D of the main features of the bifurcation diagram. When ξ/D is decreased, M^c and $M^{\rm pf}$ become indistinguishable. In the limit where $\xi/D = 0$, the critical Mach number M^c will be that of an Eulerian flow $M^c_{\rm Euler}$.

Figure 13 shows the convergence of M^c to the Eulerian critical velocity. This convergence can be characterized by fitting the polynomial law $M^c = K_1(\xi/D)^{K_2} + M^c_{\rm Euler}$ to $M^c(\xi/D)$. This fit is shown on Fig. 13 as a dotted line, yielding $K_1 = 0.322$, $K_2 = 0.615$ and $M^c_{\rm Euler} = 0.35$.

Dynamical solutions The stationary solutions obtained in the above subsection provide adequate initial data for the study of dynamical solutions. Indeed, after a small perturbation, their integration in time will generate a dynamical evolution with very small acoustic emission. Therefore, this procedure corresponds to an efficient way to start vortical dynamics in a controlled manner.

Starting from a two-vortex unstable stationary solution at a supercritical Mach

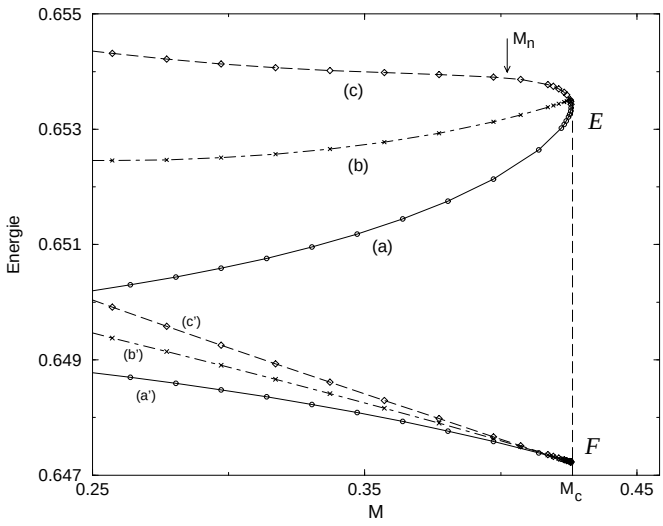

Fig. 11. Plot of the energy ($\mathcal{F}$), and functional ($\mathcal{E}$) versus Mach number ($M = |\vec{U}|/c$), with $D = 10\xi$. Stable state (a). Nucleation solutions: asymmetric branch (b) and symmetric branch (c). The diagram shows a saddle-node and a pitchfork bifurcation. The point where vortices cross the surface of the disc (see *fig.* 12) is gabelled by $M_{\rm n}$. The total fluid momentum is given by $-d\mathcal{F}/dU$ (see text).

number $M^c = 0.9$, the evolution of the NLSE time integration shows a clearly periodical emission of vortex pairs (see Fig. 12). This emission conserves total circulation.

We have studied the behavior of the frequency of vortex emission close to the bifurcation for such symmetrical wakes with different supercritical velocities (characterized by $\delta_{\rm sp} = (M - M^c)/M^c = -\delta > 0$). Our results, plotted on Fig. 14, are consistent with a $\delta_{\rm sp}^{1/2}$ scaling.

4.4.2 Subcriticality and vortex-stretching in 3D

In this section, using a 3D version of our code to integrate the NLSE, we study 3D instabilities of the basic 2D superflow.

Preparation method

We used the 2D laminar stationary solution $\psi_{0V}(x, y)$ (corresponding to branch (a) of precedent section) and the one-vortex unstable stationary solution $\psi_{1V}(x, y)$ (branch (b)) to construct the 3D initial condition

$$\psi_{\rm 3D}(x, y, z) = f_{\rm I}(z)\psi_{1V}(x, y) + [1 - f_{\rm I}(z)]\psi_{0V}(x, y). \tag{67}$$

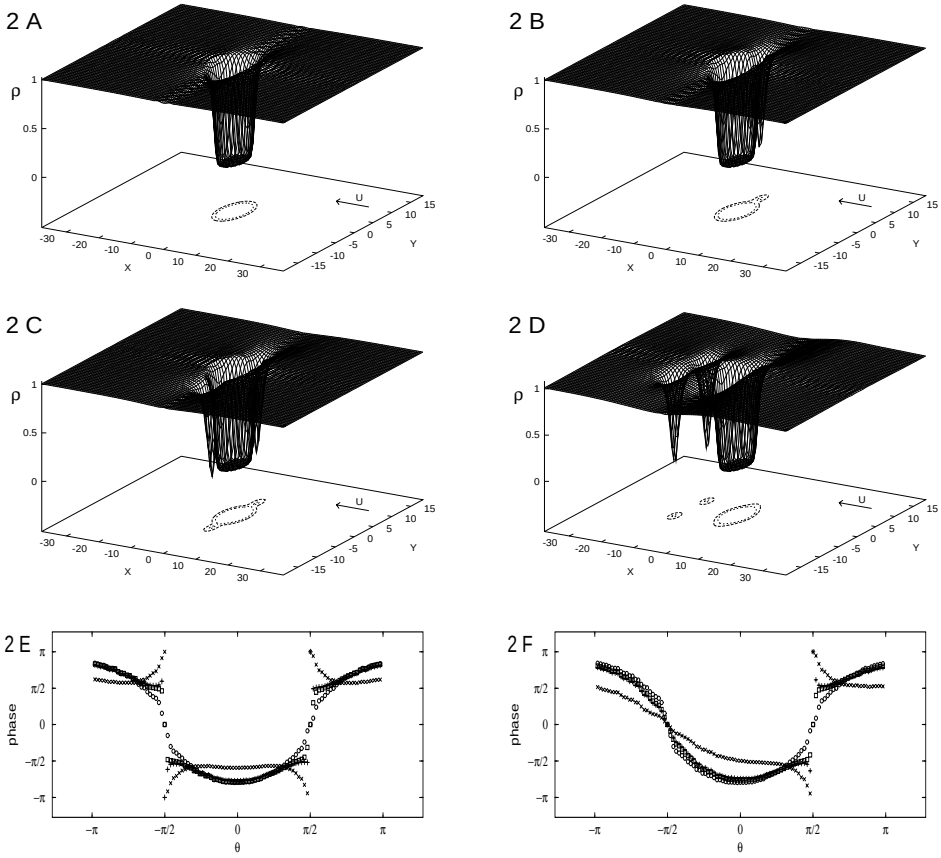

Fig. 12. Stationary states : stable (A), one vortex unstable (B), two vortices unstable (C). The surface indicates the fluid density around the cylinder ($M = 0.24, \xi/d = 0.1$). (D) Shows the result of the NLSE integration, starting from a slightly perturbed stationary (C) state. Figures (E) and (F) display the phase of the complex field ψ at the surface of the cylinder versus the polar angle θ. Asymmetric branch (A), symmetric branch (B). $M = 0.4286$ ($\circ$), $M = 0.41$ ($\Box$), $M = 0.40$ ($+$), $M = 0.30$ ($\times$). The crossing out of the vortex produces a phase discontinuity at $M^{\rm pf} \sim 0.405$.

The function $f_{\rm I}(z)$, defined by

$$f_{\rm I}(z) = (\tanh[(z - z_1)/\Delta_z] - \tanh[(z - z_2)/\Delta_z])/2,$$

takes the value 1 for $z_1 \leq z \leq z_2$ and 0 elsewhere, with Δ_z an adaptation length.

Figure 15 represents a 3D initial data prepared with this method for $\xi/D = 0.025$, $|\vec{U}|/c = 0.26$ and $\Delta_z = 2\sqrt{2}\xi$ in the $[L_x \times L_y \times L_z]$ periodicity box

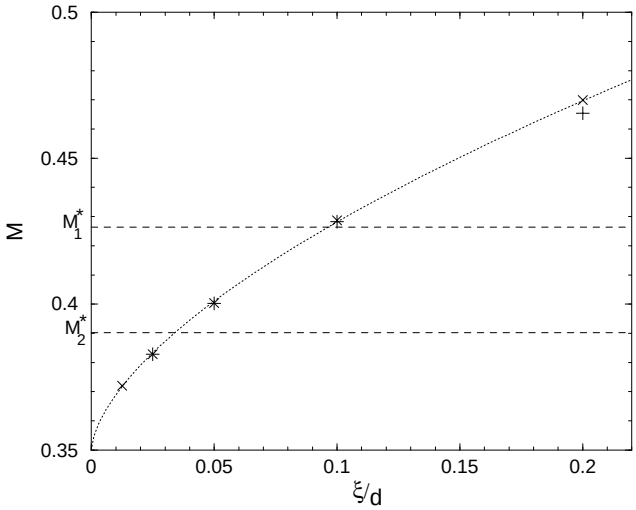

Fig. 13. Saddle-node bifurcation Mach number M^c (+) and pitchfork bifurcation Mach number $M^{\rm pf}$ ($\times$), as a function of ξ/D. The dotted curve corresponds to a fit to the polynomial law $M^c = K_1(\xi/D)^{K_2} + M^c_{\rm Euler}$ with $K_1 = 0.322$, $K_2 = 0.615$ and $M^c_{\rm Euler} = 0.35$. The dashed lines $M^*_1 \approx 0.4264$ and $M^*_2 \approx 0.3903$ correspond respectively to first and second order compressible corrections to the $M^c = 0.5$ critical velocity computed using a local sonic criterion for an incompressible flow (see text).

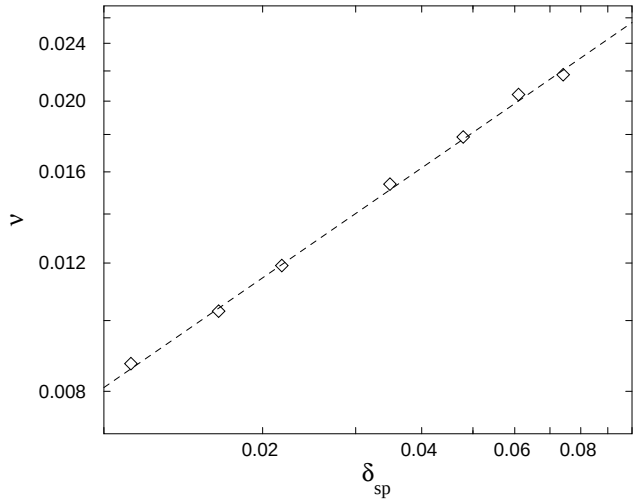

Fig. 14. Vortex emission frequency as a function of $\delta_{\rm sp} = (M - M^c)/M^c \ll 1$ (with $M^c = 0.3817$), for a symmetric wake and $\xi/D = 1/20$. The dashed line shows a fit of a polynomial $\nu = K_1\delta_{\rm sp}^{1/2}$ with $K_1 = 0.081$. The obtained $\delta_{\rm sp}^{1/2}$ law for the frequency is equivalent to the one expected for a dissipative system.

($L_x/D = 2.4\sqrt{2}\pi$, $L_y/D = 1.2\sqrt{2}\pi$ and $L_z/D = 0.4\sqrt{2}\pi$). The surface $|\psi_{\rm 3D}| = 0.5$ draws the cylinder surface and the initial condition vortex line, with both ends pinned to the right side of the cylinder.

Short time dynamics

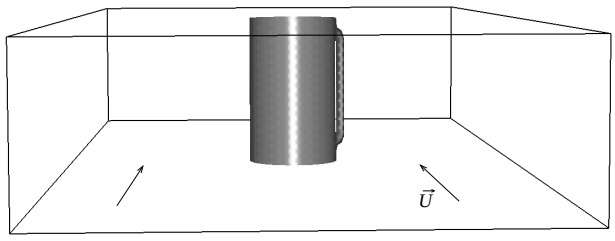

Fig. 15. Initial condition of a vortex pinned to the cylinder generated by eq.(67). The surface $|\psi_{3D}| = 0.5$ is shown for $\xi/D = 0.025$, $|\vec{U}|/c = 0.26$ and $\Delta_z = 2\sqrt{2}\xi$ in the $[L_x \times L_y \times L_z]$ periodicity box ($L_x/D = 2.4\sqrt{2}\pi$, $L_y/D = 1.2\sqrt{2}\pi$ and $L_z/D = 0.4\sqrt{2}\pi$).

Starting from the initial condition (67), the evolution of the NLSE time integration shows a short-time and a long-time dynamics.

During the short-time dynamics, the initial pinned vortex line rapidly contracts, evolving through a decreasing number of half-ring-like loops, down to a single quasi-stationary half-ring (see Figs. 16a, 16b, 16c). This evolution happens mainly on the plane perpendicular to the flow, provided that the initial vortex is long enough to contract to a quasi-stationary half-ring as shown on Fig. 16c. Otherwise, the vortex line collapses against the cylinder while moving upstream.

Note that this quasi-stationary half-ring has been used by Varoquaux [42,43] to estimate the nucleation barrier in a 3D experiment.

The dynamics of the half-ring situation (Fig. 16c) is very slow and can be shown to be close to a stationary field. Indeed, the local flow velocity v in an Eulerian flow around a cylindrical obstacle is known to vary from $v = |\vec{U}|$ at infinity to $v = 2|\vec{U}|$ at both sides of its surface. Moreover, the diameter d of a stationary vortex ring in an infinite Eulerian flow with no obstacle is given by [1]:

$$|\vec{U}|/c = (\sqrt{2}\xi/d)\left[\ln(4d/\xi) - K\right], \tag{68}$$

where $|\vec{U}|$ is the flow velocity at infinity and the vortex core model constant $K \sim 1$ is obtained by fitting the numerical results in [44]. Therefore, for the values used on Figs. 16, we expect that local velocities range from $v = 0.25$ to $v = 2 \times 0.25$. Equation (68) thus implies that the diameter of an hypothetical stationary half-ring should be bounded by $d(v = |\vec{U}| = 0.25) = 18.8\xi$ and $d(v = 2|\vec{U}| = 0.5) = 6.3\xi$. The diameter $d \approx 9\xi$ measured on the half-ring observed on Fig. 16c is consistent with its quasi-stationary behavior. Similarly the diameter of the half-ring shown on Fig. 18 $d \approx 7.6\xi$ is also found to be between the corresponding bounds $d(0.35) = 11.4\xi$ and $d(2 \times 0.35) = 3\xi$.

Vortex stretching as a subcritical drag mechanism A small perturbation

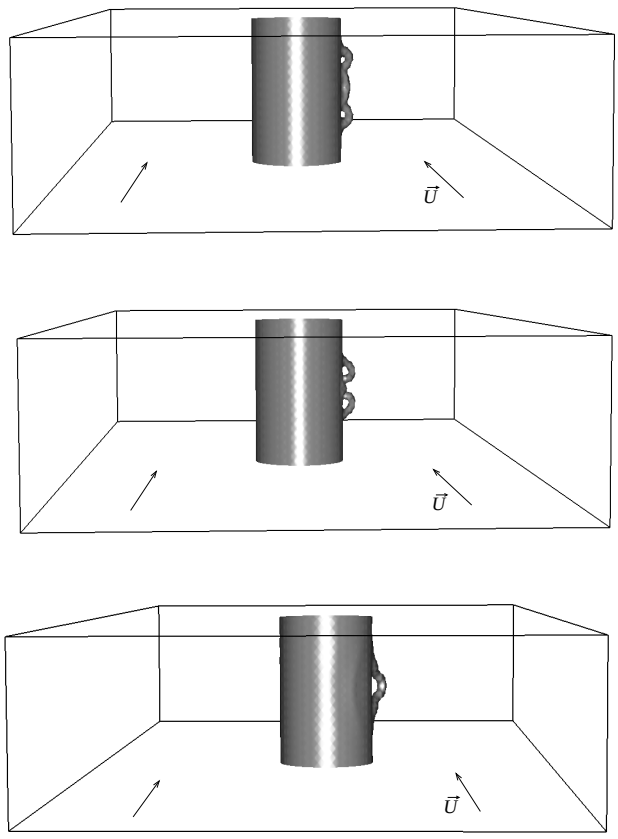

Fig. 16. Short-time dynamics for $\xi/D = 1/40$ and $|\vec{U}|/c = 0.25$ starting from Fig. 15: A ($t = 5\xi/c$), B($t = 10\xi/c$) and C($t = 15\xi/c$). The contraction of the initial vortex line occurs in the plane perpendicular to the flow. The half-rings have a diameter compatible with that of a quasi-stationary half-ring (see text).

over the half-ring solution can drive the system into two opposite situations where the half-ring either starts moving upstream or downstream.

When driven upstream, the half-ring eventually collapses against the cylinder, dissipating its energy as sound waves. Otherwise, the vortex loop is stretched while the pinning points move towards the back of the cylinder. Figures 17 show the long-time dynamics for a stretching case with $\xi/D = 1/40$ and $|\vec{U}|/c = 0.25$ starting from Fig. 16c. Figure 19 shows a later situation for $\xi/D = 1/20$ and $|\vec{U}|/c = 0.35$ starting from Fig. 18. As the vortex loop grows, its backmost part remains oblique to the flow. The described vortex stretching mechanism consumes energy, thus generating drag. It can be responsible for the appearance of drag in experimental superflows if fluctuations are strong enough to nucleate the initial vortex loop (which is imposed extrinsically in our numerical system). Note that it takes place for 2D subcritical velocities.

Figure 20 displays several numerical and experimental [45] critical Mach num-

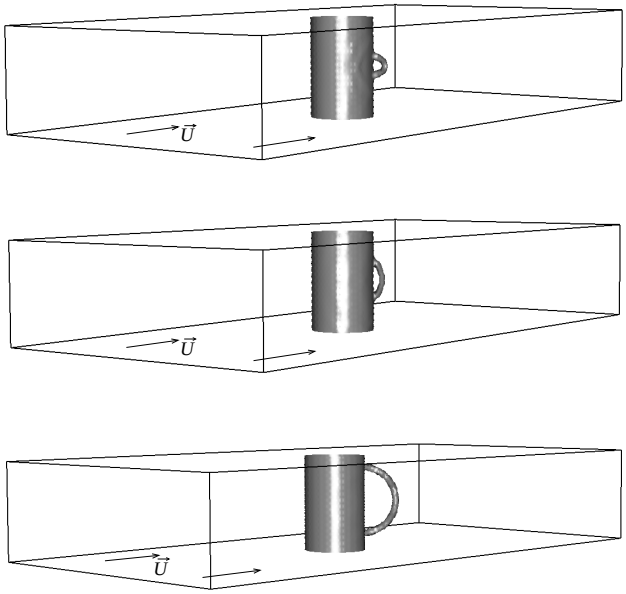

Fig. 17. Long-time dynamics for $\xi/D = 1/40$ and $|\vec{U}|/c = 0.25$ starting from Fig. 16c. The half-ring moves downstream while growing.

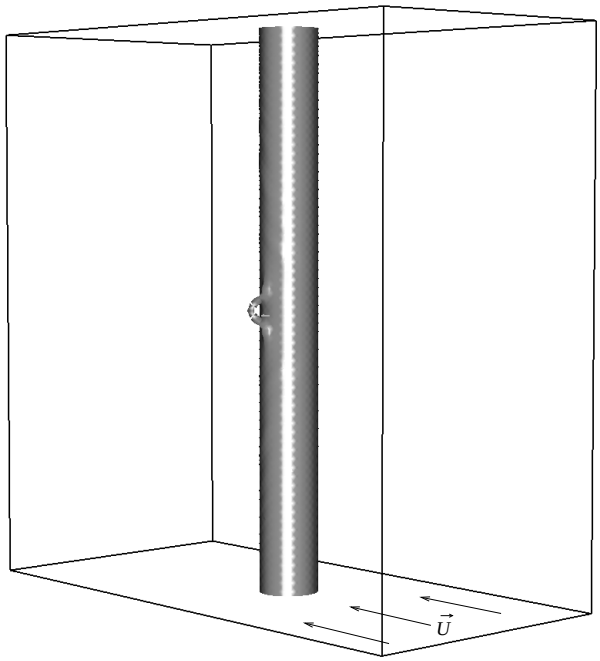

Fig. 18. Quasi-nucleation solution for $|\vec{U}|/c = 0.35$ and $\xi/D = 1/20$ at time $t = 15\xi/c$.

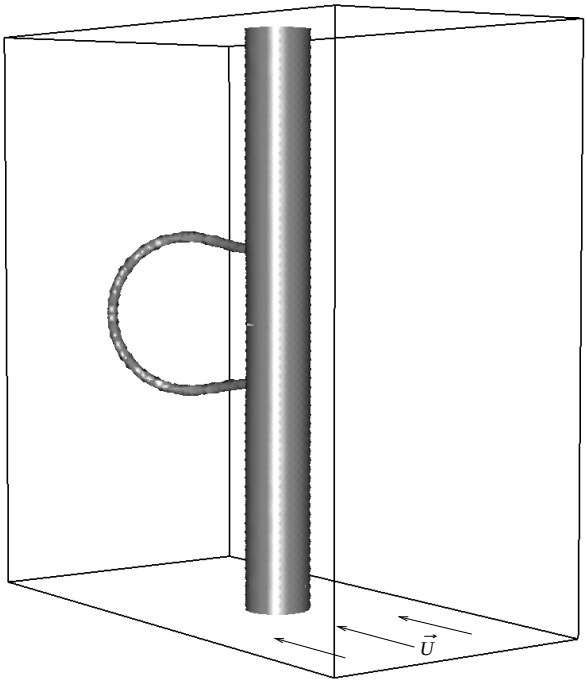

Fig. 19. Vortex stretching at $t = 150\xi/c$ with $|\vec{U}|/c = 0.35$ and $\xi/D = 1/20$. The vortex line is oblique to the flow.

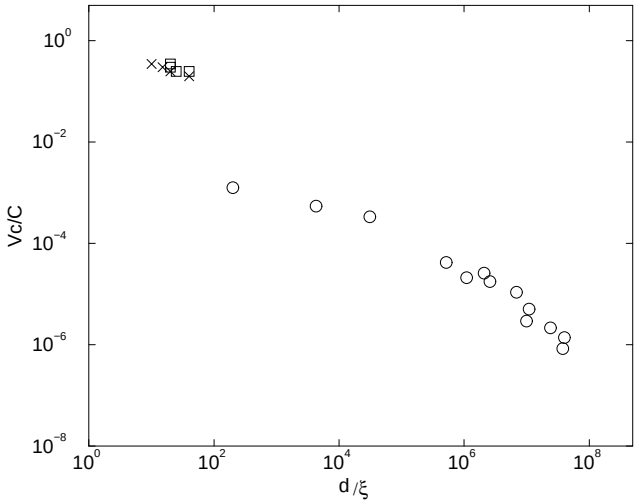

Fig. 20. Critical Mach number V_c/C versus scale ratio of numerical and experimental data D/ξ. Circles correspond to several experiments from [45]. Squares stand for our numerical stretching cases while crosses correspond to non-stretching cases [14].

bers (V_c/C) with respect to D/ξ, which seem to follow a (-1) slope in a log-log plot. The squares stand for our numerical stretching cases while the crosses correspond to non-stretching cases. There is a frontier between the 3D numerical dissipative and non-dissipative cases [14]. For $1/30 < \xi/D < 1/20$,

the frontier corresponds to the expression $R_s = 5.5$ with

$$R_s \equiv |\vec{U}|D/c\xi = MD/\xi. \tag{69}$$

This superfluid 'Reynolds' number is defined in the same way as the standard (viscous) Reynolds number $Re \equiv |\vec{U}|D/\nu$ (with ν the kinematic viscosity). It has been shown, in the superfluid turbulent ($R_s \gg 1$) regime, that R_s is equivalent to the standard (viscous) Reynolds number Re [10,9,11]. Note that, for a Bose condensate of particles of mass m, the quantum of velocity circulation around a vortex, $\Gamma = 2\pi\sqrt{2}c\xi$, has the Onsager-Feynman value $\Gamma = h/m$ (h is Planck's constant) and the same physical dimensions L^2T^{-1} as ν.

The value of R_s divides the space of parameters into a laminar flow zone and a recirculating flow zone, very much like in the problem of a circular disc in a viscous fluid in which this frontier is also found to be around $Re \sim 5$. It therefore seems to exist some degree of universality between viscous normal fluids and superfluids modeled by NLSE as discussed in [10,9,11]. In the context of superfluid ^{4}He flow, the experimental critical velocity is known to depend strongly on the system's characteristic size D. It is often found to be well below the Landau value (based on the velocity of roton excitation) except for experiments where ions are dragged in liquid helium. Feynman's alternative critical velocity criterion $Rs \sim \log(D/\xi)$ is based on the energy needed to form vortex lines. It produces better estimates for various experimental settings, but does not describe the vortex nucleation mechanism [1].

In a recent experiment, Raman *et al.* have studied dissipation in a Bose-Einstein condensed gas by moving a blue detuned laser beam through the condensate at different velocities [46]. In their inhomogeneous condensate, they observed a critical Mach number for the onset of dissipation $M^c_{2D}/1.6$.

Our computations were performed for values of ξ/D comparable to those in Bose-Einstein condensed gas experiments. They demonstrate the possibility of a subcritical drag mechanism, based on 3D vortex stretching. It would be very interesting to determine experimentally the dependence of the critical Mach number on the parameter ξ/D and the nature (2D or 3D) of the excitations [14].

4.5 Stability of attractive Bose-Einstein condensates

In this section, following reference [15], we study condensates with attractive interactions which are known to be metastable in spatially localized systems, provided that the number of condensed particles is below a critical value $\mathcal{N}_c$ [7]. Various physical processes compete to determine the lifetime of attractive

condensates. Among them one can distinguish macroscopic quantum tunneling (MQT) [47,48], inelastic two and three body collisions (ICO) [49,50] and thermally induced collapse (TIC) [48,51]. We compute the life-times, using both a variational Gaussian approximation and the exact numerical solution for the condensate wave-function.

4.5.1 Computations of stationary states

Gaussian approximation

A Gaussian approximation for the condensate density can be obtained analytically through the following procedure.

Inserting

$$\psi(r,\tilde{t}) = A(\tilde{t}) \exp\left(-r^2/2r_{\rm G}^2(\tilde{t}) + ib(\tilde{t})r^2\right) \tag{70}$$

into the action (45), where $\mathcal{F}$ is given by (52), yields a set of Euler-Lagrange equations for $r_{\rm G}(\tilde{t})$, $b(\tilde{t})$ and the (complex) amplitude $A(\tilde{t})$. The stationary solutions of the Euler-Lagrange equations produce the following values [52]:

$$\mathcal{N}(\mu) = \frac{4\sqrt{2\pi^3}\left(-8\mu + 3\sqrt{7+4\mu^2}\right)}{7|\tilde{a}|\left(-2\mu+\sqrt{7+4\mu^2}\right)^{3/2}}, \tag{71}$$

$$\mathcal{E} = \mathcal{N}(\mu)\left(-\mu + 3\sqrt{7+4\mu^2}\right)/7. \tag{72}$$

$\mathcal{N}$ is found to be maximal at $\mathcal{N}_c^G = 8\sqrt{2\pi^3}/|5^{5/4}\tilde{a}|$. The corresponding value of the chemical potential is $\mu = \mu_c^G = 1/2\sqrt{5}$.

Linearizing the Euler-Lagrange equations around the stationary solutions, yields the following expression for the eigenvalues [52]:

$$\lambda^2(\mu) = 8\mu^2 - 4\mu\sqrt{7+4\mu^2} + 2 \tag{73}$$

This qualitative behavior is the generic signature of a Hamiltonian Saddle Node (HSN) bifurcation defined, at lowest order, by the normal form [53]

$$m_{eff}\ddot{Q} = \delta - \beta Q^2, \tag{74}$$

where $\delta = (1 - \mathcal{N}/\mathcal{N}_c)$ is the bifurcation parameter. The critical amplitude Q is related to the radius of the condensate [52]. We can relate the parameters β and m_{eff} to critical scaling laws, by defining the appropriate energy

$$\mathcal{E} = \mathcal{E}_0 + m_{\rm eff}\dot{Q}^2/2 - \delta\ Q + \beta Q^3/3 - \gamma\delta. \tag{75}$$

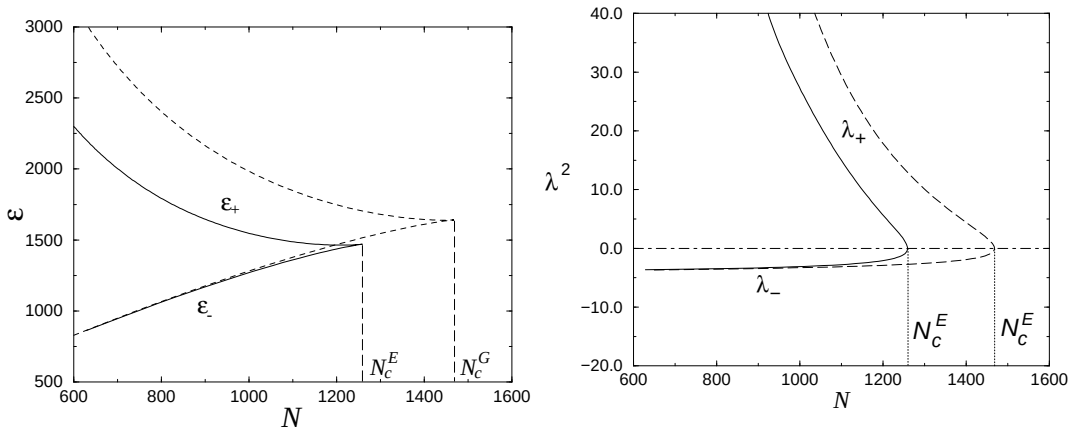

Fig. 21. Stationary solutions of the NLSE equation versus particle number $\mathcal{N}$. Left: value of the energy functional $\mathcal{E}_+$ on the stable (elliptic) branch and $\mathcal{E}_-$ on the unstable (hyperbolic) branch. Right: square of the bifurcating eigenvalue ($\lambda_\pm^2$); $|\lambda_-|$ is the energy of small excitations around the stable branch. Solid lines: exact solution of the NLSE equation. Dashed lines: Gaussian approximation.

From (74) it is straightforward to derive, close to the critical point $\delta = 0$, the universal scaling laws

$$\mathcal{E}_\pm = \mathcal{E}_c - \mathcal{E}_l \delta \pm \mathcal{E}_\Delta \delta^{3/2}, \tag{76}$$

$$\lambda_\pm^2 = \pm \lambda_\Delta^2 \delta^{1/2}, \tag{77}$$

where $\mathcal{E}_c = \mathcal{E}_0$, $\mathcal{E}_l = \gamma$, $\mathcal{E}_\Delta = 2/3\sqrt{\beta}$ and $\lambda_\Delta^2 = 2\sqrt{\beta}/m_{eff}$.

Numerical branch following

Using the branch-following method described in section 4.3, we have computed the exact stationary solutions of the NLSE. We use the following value $\tilde{a} = -5.74 \times 10^{-3}$, that corresponds to experiments with ^{7}Li atoms in a radial trap [54,7].

As apparent on Fig. 3, the exact critical $\mathcal{N}_c^E = 1258.5$ is smaller than the Gaussian one $\mathcal{N}_c^G = 1467.7$ [55,47]. The critical amplitudes corresponding to the Gaussian approximation can be computed from (71) and (72). One finds $\mathcal{E}_c = 4\sqrt{2\pi^3}/|5^{3/4}\tilde{a}|$, $\mathcal{E}_\Delta = 64\sqrt{\pi^3}/|5^{9/4}\tilde{a}|$ and $\lambda_\Delta^2 = 4\sqrt{10}$. For the exact solutions, we obtain the critical amplitudes by performing fits on the data. One finds $\mathcal{E}_\Delta = 1340$ and $\lambda_\Delta^2 = 14.68$. Thus, the Gaussian approximation captures the bifurcation qualitatively, but with quantitative 17% error on N_c [55], 24% error on $\mathcal{E}_\Delta$ and 14% error on λ_Δ^2. Fig. 4 shows the physical origin of the quantitative errors in the Gaussian approximation. By inspection it is apparent that the exact solution is well approximated by a Gaussian only for small $\mathcal{N}$ on the stable (elliptic) branch.

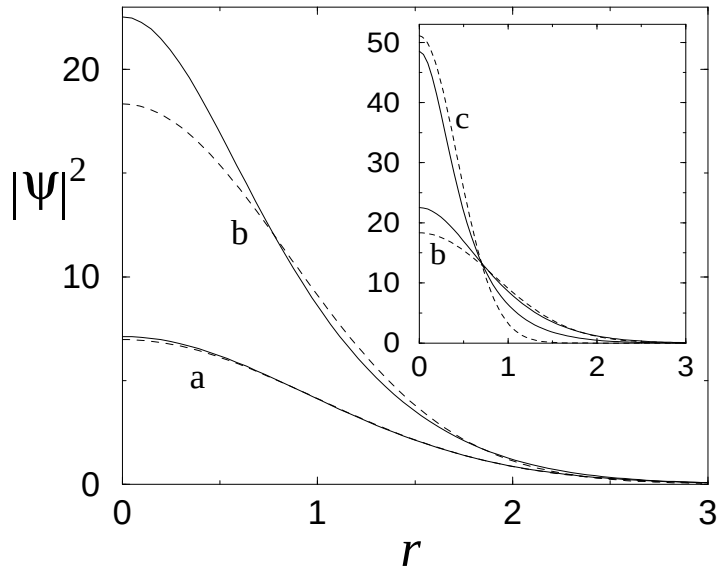

Fig. 22. Condensate density $|\psi|^2$ versus radius r, in reduced units (see text). Solid lines: exact solution of the NLSE equation. Dashed lines: Gaussian approximation. Stable (elliptic) solutions are shown for particle number $\mathcal{N} = 252$ (a) and $\mathcal{N} = 1132$ (b). (c) is the unstable (hyperbolic) solution for $\mathcal{N} = 1132$ (see insert).

4.5.2 Estimation of life-times

In this section, we estimate the decay rates due to thermally induced collapse, macroscopic quantum tunneling and inelastic collisions.

Thermally induced collapse

The thermally induced collapse (TIC) rate Γ_T is estimated using the formula [56]

$$\frac{\Gamma_T}{\omega} = \frac{|\lambda_+|}{2\pi} \exp\left[\frac{-\hbar\omega\,(\mathcal{E}_+ - \mathcal{E}_-)}{k_B T}\right] \tag{78}$$

where $\hbar\omega(\mathcal{E}_+ - \mathcal{E}_-)$ is the (dimensionalized) height of the nucleation energy barrier, T is the temperature of the condensate and k_B is the Boltzmann constant. Note that the prefactor characterizes the typical decay time which is controlled by the slowest part of the nucleation dynamics: the top-of-the-barrier saddle point eigenvalue λ_+. The behavior of Γ_T can be obtained directly from the universal saddle-node scaling laws (76) and (77). Thus the exponential factor and the prefactor vanish respectively as $\delta^{3/2}$ and $\delta^{1/4}$.

Macroscopic quantum tunneling

We estimate the MQT decay rate using an instanton technique that takes into account the semi classical trajectory giving the dominant contribution to the

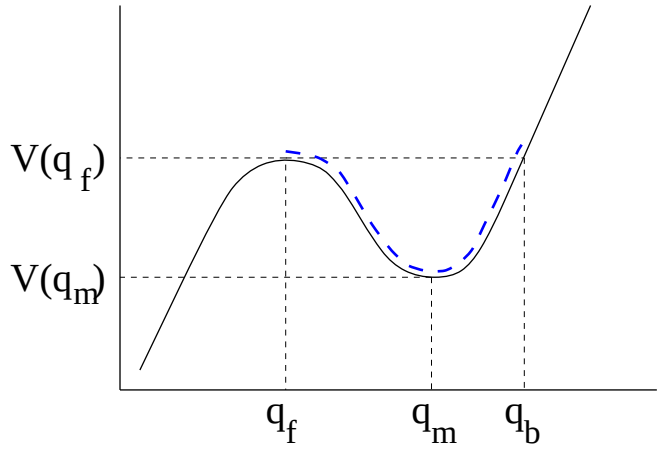

Fig. 23. The bounce trajectory is shown as dashes, above the potential $V(q)$.

quantum action path integral [48,47]. This trajectory is approximated as the solution of

$$\frac{d^2q(t)}{dt^2} = -\frac{dV(q)}{dq}, \tag{79}$$

$V(q)$ is a polynomial such that $-V(q)$ reconstructs the Hamiltonian dynamics. $V(q)$ is determined by the relations

$$V(q_m) = -\mathcal{E}_+ \tag{80}$$
$$V(q_f) = -\mathcal{E}_- \tag{81}$$
$$\partial_q^2 V(q_m) = |\lambda_+(\mathcal{N})| \tag{82}$$
$$\partial_q^2 V(q_f) = -|\lambda_-(\mathcal{N})|. \tag{83}$$

The bounce trajectory is displayed on Fig. 23 (dashed line) above the potential $V(q)$. The MQT rate is estimated as

$$\frac{\Gamma_Q}{\omega} = \sqrt{\frac{|\lambda_-|v_0^2}{4\pi}} \exp\left[\frac{-4}{\sqrt{2}}\int_{q_f}^{q_b}\sqrt{V(q)-V(q_f)}dq\right], \tag{84}$$

where v_0 is defined by the asymptotic form of the bounce trajectory $q(t)$ [48]: $q(\tau) \sim q_f + (v_0/|\lambda_-|)\exp[-|\lambda_-\tau|]$. Universal scaling laws can be derived close to criticality from (74), (76) and (77). The exponential factor in (84) follows the same scaling than $\sqrt{|\mathcal{E}_+ - \mathcal{E}_-|}dq$. It therefore vanishes as $\delta^{5/4}$. From the asymptotic form of $q(t)$, dq follows the same law as $v_0/|\lambda_-|$. Thus $v_0 \sim \delta^{3/4}$ and the prefactor vanishes as $\delta^{7/8}$.

Inelastic collision

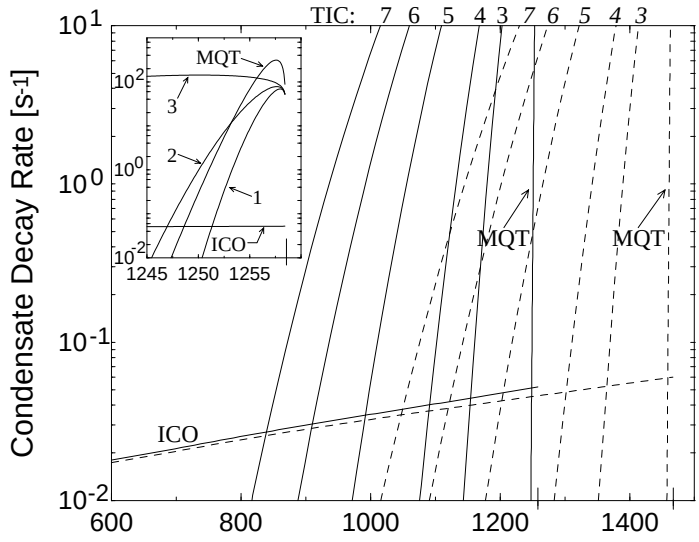

Fig. 24. Condensate decay rates versus particle number. ICO: inelastic collisions. MQT: macroscopic quantum tunneling TIC: thermally induced collapse at temperatures $1nK$ (1),$2nK$(2), $50nK$ (3), $100nK$ (4), $200nK$ (5), $300nK$ (6) and $400nK$ (7). The insert shows the details of the cross-over region between quantum tunneling and thermal decay rate. Solid lines: exact solution of the NLSE equation, dashed lines: Gaussian approximation.

The inelastic collision rate (ICO) is estimated using the relation

$$\frac{d\mathcal{N}}{dt} = f_C(\mathcal{N}) \tag{85}$$

with

$$f_C(\mathcal{N}) = K \int |\psi|^4 d^3\tilde{\mathbf{x}} + L \int |\psi|^6 d^3\tilde{\mathbf{x}}, \tag{86}$$

where $K = 3.8 \times 10^{-4}\,\mathrm{s}^{-1}$ and $L = 2.6 \times 10^{-7}\,\mathrm{s}^{-1}$. The ICO rate can be evaluated from the stable branch alone. In order to compare the particle decay rate $f_C(\mathcal{N})$ to the condensate collective decay rates obtained for TIC and MQT, we compute the condensate ICO half-life as:

$$\tau_{1/2}(\mathcal{N}) = \int_{\mathcal{N}/2}^{\mathcal{N}} dn / f_C(n) \tag{87}$$

and plot $\tau_{1/2}^{-1}$

Discussion

It is apparent by inspection of Fig. 6 that for a given value of $\mathcal{N}$ the exact and Gaussian approximate rates are dramatically different. We now compare the relative importance of the different exact decay rates. At $T \leq 1\,\mathrm{nK}$ the MQT

effect becomes important compared to the ICO decay in a region very close to $\mathcal{N}_c^E$ ($\delta \leq 8 \times 10^{-3}$) as it was shown in [47] using Gaussian computations but evaluating them with the exact maximal number of condensed particles $\mathcal{N}_c^E$. Considering thermal fluctuations for temperatures as low as 2 nK, it is apparent on Fig. 6 (see insert) that the MQT will be the dominant decay mechanism only in a region extremely close to $\mathcal{N}_c$ ($\delta < 5 \times 10^{-3}$) where the condensates will live less than 10^{-1} s. Thus, in the experimental case of ^{7}Li atoms, the relevant effects are ICO and TIC, with cross-over determined in Fig. 6.

5 Conclusion

The main result of the NLSE simulations presented in section 3.2 is that two diagnostics of Kolmogorov's regime in decaying turbulence are satisfied. These diagnostics are, at the time of the maximum of energy dissipation: (i) a parameter-independent kinetic energy dissipation rate and (ii) a $k^{-5/3}$ spectral scaling in the inertial range. Thus, the NLSE simulations were shown to be very similar, as far as energetics is concerned, with the viscous simulations. The experimental results shown in section 3.3 show that the Kolmogorov cascade survives in the superfluid regime.

We have seen that the numerical tools developed in section 4.3 can be used in practice to obtain the stationary solutions of the NLSE. These methods have allowed us to find the full bifurcation diagrams of Bose-Einstein condensates with attractive interactions and superflows past a cylinder. Furthermore, the stationary solutions have given us efficient way to start vortical dynamics (in 2D and 3D) in a controlled manner.

6 Acknowledgments

The work reviewed in this paper was performed in collaboration with M. Abid, G. Dewel, C. Huepe, J. Maurer, S. Metens, C. Nore, C-T. Pham and P. Tabeling. Computations were performed at the Institut du Développement et des Ressources en Informatique Scientifique.

References

[1] R. J. Donnelly. *Quantized Vortices in Helium II.* Cambridge Univ. Press, Cambridge, 1991.

[2] E.P. Gross. Structure of a quantized vortex in boson systems. *Nuovo Cimento*, 20(3), 1961.

[3] L.P. Pitaevskii. Vortex lines in an imperfect Bose gas. *Sov. Phys.-JETP*, 13(2), 1961.

[4] L. Landau and E. Lifchitz. *Fluid Mechanics*. Pergamon Press, Oxford, 1980.

[5] M. H. Anderson, J. R. Ensher, M. R. Matthews, C. E. Wieman, and E. A. Cornell. *Science*, 269:198, 1995.

[6] K. B. Davis, M. O. Mewes, M. R. Adrews, N. J. van Druten, D. S. Durfee, D. M. Kurn, and W. Ketterle. *Phys. Rev. Lett.*, 75:3969, 1995.

[7] C. C. Bradley, C. A. Sackett, and R. G. Hulet. Bose-einstein condensation of lithium: Observation of limited condensate number. *Phys. Rev. Lett.*, 78(6):985, 1997.

[8] Franco Dalfovo, Stefano Giorgini, Lev P. Pitaevskii, and Sandro Stringari. Theory of bose-einstein condensation in trapped gases. *Reviews of Modern Physics*, 71(3), 1999.

[9] C. Nore, M. Abid, and M. Brachet. Decaying kolmogorov turbulence in a model of superflow. *Phys. Fluids*, 9(9):2644, 1997.

[10] C. Nore, M. Abid, and M. E. Brachet. Kolmogorov turbulence in low-temperature superflows. *Phys. Rev. Lett.*, 78(20):3896–3899, 1997.

[11] M. Abid, M. Brachet, J. Maurer, C. Nore, and P. Tabeling. Experimental and numerical investigations of low–temperature superfluid turbulence. *Eur. J. Mech. B Fluids*, 17(4):665–675, 1998.

[12] C. Huepe and M.-E. Brachet. Solutions de nucléation tourbillonnaires dans un modèle d'écoulement superfluide. *C. R. Acad. Sci. Paris*, 325(II):195–202, 1997.

[13] C. Huepe and M. E. Brachet. Scaling laws for vortical nucleation solutions in a model of superflow. *Physica D*, 140:126–140, 2000.

[14] C. Nore, C. Huepe, and M. E. Brachet. Subcritical dissipation in three-dimensional superflows. *Phys. Rev. Lett.*, 84(10):2191, 2000.

[15] C. Huepe, S. Métens, G. Dewel, P. Borckmans, and M.-E. Brachet. Decay rates in attractive bose-einstein condensates. *Phys. Rev. Lett.*, 82(2):1616, 1999.

[16] E. A. Spiegel. Fluid dynamical form of the linear and nonlinear schrödinger equations. *Physica D*, 1:236, 1980.

[17] P. Nozières and D. Pines. *The Theory of Quantum Liquids.* Addison Wesley, New York, 1990.

[18] C. Nore, M. Brachet, and S. Fauve. Numerical study of hydrodynamics using the nonlinear schrödinger equation. *Physica D*, 65:154–162, 1993.

[19] D. Gottlieb and S. A. Orszag. *Numerical Analysis of Spectral Methods.* SIAM, Philadelphia, 1977.

[20] M. P. Kawatra and R. K. Pathria. Quantized vortices in imperfect bose gas. *Phys.Rev.*, 151:1, 1966.

[21] K. W. Schwarz. Three-dimensional vortex dynamics in superfluid ^{4}he: line-line and line-boundary interactions. *Phys. Rev. B*, 31:5782, 1985.

[22] J. C. Neu. Vortices in complex scalar fields. *Physica D*, 43:385, 1990.

[23] F. Lund. Defect dynamics for the nonlinear schrödinger equation derived from a variational principle. *Phys.Rev.Lett.*, A 159:245, 1991.

[24] G. I. Taylor and A. E. Green. Mechanism of the production of small eddies from large ones. *Proc. Soc. Lond. A*, 158:499, 1937.

[25] M. E. Brachet, D. I. Meiron, S. A. Orszag, B. G. Nickel, R. H. Morf, and U. Frisch. Small-scale structure of the taylor-green vortex. *J. Fluid Mech.*, 130:411–452, 1983.

[26] M. Brachet. Géométrie des structures à petite échelle dans le vortex de taylor-green. *C.R.A.S II*, **311**:775, 1990.

[27] J. Domaradzki, W. Liu, and M. Brachet. An analysis of sugrid-scale interactions in numerically simulated isotropic turbulence. *Phys. Fluids A*, 5:1747, 1993.

[28] C. Nore, M. Abid, and M. Brachet. Simulation numérique d'écoulements cisaillés tridimensionnels à l'aide de l'équation de schrödinger non linéaire. *C.R.A.S*, 319 II(7):733, 1994.

[29] U. Frisch. *Turbulence, the legacy of A. N. Kolmogorov.* Cambridge Univ. Press, Cambridge, 1995.

[30] S. Douady, Y. Couder, and M. E. Brachet. Direct observation of the intermittency of intense vorticity filaments in turbulence. *Phys. Rev. Lett.*, 67:983, 1991.

[31] G. Zocchi, P. Tabeling, J. Maurer, and H. Willaime. Measurement of the scaling of the dissipation at high reynolds numbers. *Phys. Rev. E*, 50:3693, 1994.

[32] S. Fauve, C. Laroche, and B. Castaing. Pressure fluctuations in swirling turbulent flows. *J. Phys. II*, 3:271, 1993.

[33] F. Belin, P. Tabeling, and H. Willaime. Exponents of the structure functions in a low temperature helium experiment. *Physica D*, 93:52–63, 1996.

[34] V. Hakim. Nonlinear Schrödinger flow past an obstacle in one dimension. *Phys. Rev. E*, 55(3):2835–2845, 1997.

[35] T. Tsuzuki. Nonlinear waves in the Pitaevskii-Gross equation. *J. Low Temp. Phys.*, 4(4), 1971.

[36] V.E. Zakharov and A.B. Shabat. Interaction between soliton in a stable medium. *Sov. Phys.-JETP*, 37(5):823–828, 1973.

[37] R. Seydel. *From Equilibrium to Chaos: Practical Bifurcation and Stability Analysis*. Elsevier, New York, 1988.

[38] C. Mamun and L. Tuckerman. Asymmetry and hopf bifurcation in spherical couette flow. *Phys. Fluids*, 7(1):80, 1995.

[39] W. Press, S. Teukolsky, W. Vetterling, and B.Flannery. *Numerical Recipres in Fortran*. Cambridge Univ. Press, Cambridge, 1994.

[40] R. Klein and A. J. Majda. Self-stretching of perturbed vortex filaments. *Physica D*, 53:267, 1991.

[41] T. Frisch, Y. Pomeau, and S. Rica. Transition to dissipation in a model of superflow. *Phys.Rev.Lett.*, 69:1644, 1992.

[42] O. Avenel, G.G. Ihas, and E. Varoquaux. The nucleation of vortices in superfluid ^{4}he: Answers and questions. *J. Low Temp.Phys.*, 93:1031–1057, 1993.

[43] G.G. Ihas, O. Avenel, R. Aarts, R Salmelin, and E. Varoquaux. *Phys. Rev. Lett.*, 69(2):327, 1992.

[44] C. A. Jones and P. H. Roberts. *J. Phys. A*, 15:2599, 1982.

[45] J. Wilks. *The properties of liquid and solid helium*. Clarendon Press, Oxford, 1967.

[46] C. Raman, M. Köhl, R. Onofrio, D.S. Durfee a nd C.E. Kuklewicz, Z. Hadzibabic, and W. Ketterle. Evidence for a critical velocity in a bose-einstein con densed gas. *Phys. Rev. Lett.*, 83(13):2502, 1999.

[47] M. Ueda and A. J. Leggett. Macroscopic quantum tunneling of a bose-einstein condensate with attractive interaction. *Phys. Rev. Lett.*, 80(8):1576, 1998.

[48] H. T. C. Stoof. Macroscopic quantum tunneling of a bose condensate. *J. Stat. Phys.*, 87:1353, 1997.

[49] H. Shi and W.-M. Zheng. Bose-einstein condensation in an atomic gas with attractive interactions. *Phys. Rev. A*, 55(4):2930, 1997.

[50] R. J. Dodd, Mark Edwards, C. J. Williams, C. W. Clark, M. J. Holland, P. A. Ruprecht, and K. Burnett. Role of attractive interactions on bose-einstein condensation. *Phys. Rev. A*, 54(1):661, 1996.

[51] C. A. Sackett, H. T. C. Stoof, and R. G. Hulet. Growth and collapse of a bose-einstein condensate with attractive interactions. *Phys. Rev. Lett.*, 80(10):2031, 1998.

[52] C. Huepe. *Bifurcations et instabilités dans les condensats de Bose-Einstein et les écoulements superfluides*. PhD thesis, Ecole Normale Supeérieure, 1999.

[53] J. Guckenheimer and P. Holmes. *Nonlinear Oscillations, Dynamical Systems and Bifurcations of Vector Fields*. Springer-Verlag, Berlin, 1983.

[54] C. C. Bradley, C. A. Sackett, J. J. Tollett, and R. G. Hulet. Evidence of bose-einstein condensation in an atomic gas with attractive interactions. *Phys. Rev. Lett.*, 75(9):1687, 1995.

[55] P. A. Ruprecht, M. J. Holland, K. Burnett, and Mark. Edwards. Time-dependent solution of the nonlinear schrödinger equation for bose-condensed trapped neutral atoms. *Phys. Rev. A*, 51(6):4704, 1995.

[56] C.W. Gardiner. *Handbook of Stochastic Methods*. Springer-Verlag, Berlin, 1985.